



1 **Beyond the pixel: using patterns and multiscale spatial information to improve the
2 retrieval of precipitation from space-borne passive microwave imagers**

4 Clément Guilloteau^{1*} and Efi Foufoula-Georgiou^{1,2}

5 ¹ Department of Civil and Environmental Engineering, University of California, Irvine

6 ² Department of Earth System Science, University of California, Irvine

7 *: cguillot@uci.edu

9 **Abstract**

11 The quantitative estimation of precipitation from orbiting passive microwave imagers
12 has been performed for more than 30 years. The development of retrieval methods consists of
13 establishing physical or statistical relationships between the brightness temperatures (TBs)
14 measured at frequencies between 5 and 200 GHz and precipitation. Until now, these
15 relationships have essentially been established at the “pixel” level, associating the average
16 precipitation rate inside a pre-defined area (the pixel) to the collocated multispectral radiometric
17 measurement. This approach considers each pixel as an independent realization of a process
18 and ignores the fact that precipitation is a dynamic variable with rich multiscale spatial and
19 temporal organization. Here we propose to look beyond the pixel values of the TBs, and show
20 that useful information for precipitation retrieval can be derived from the variations of the
21 observed TBs in a spatial neighborhood around the pixel of interest. We also show that
22 considering neighboring information allows to better handle the complex observation geometry
23 of conical-scanning microwave imagers, involving frequency-dependent beamwidths,

1

Early Online Release: This preliminary version has been accepted for publication in *Journal of Atmospheric and Oceanic Technology*, may be fully cited, and has been assigned DOI 10.1175/JTECH-D-19-0067.1. The final typeset copyedited article will replace the EOR at the above DOI when it is published.

24 overlapping fields of view and large Earth incidence angles. Using spatial convolution filters,
25 we compute “nonlocal” radiometric parameters sensitive to spatial patterns and scale-dependent
26 structures of the TB fields which are the “geometric signatures” of specific precipitation
27 structures such as convective cells. We demonstrate that using nonlocal radiometric parameters
28 to enrich the spectral information associated to each pixel allows for reduced retrieval
29 uncertainty (reduction of 6 to 11% of the mean absolute retrieval error) in a simple k -nearest
30 neighbors retrieval scheme.

31

32 **1. Introduction**

33 Since the first experimental algorithms developed for the SMMR (see appendix A for
34 all acronyms used in this article) imager in the 1980’s, the algorithms performing the retrieval
35 of precipitation from passive microwave imagers in orbit have been continuously evolving and
36 improving [Wilheit and Chang 1980, Spencer 1986, Spencer et al. 1989, Wilheit et al. 1991,
37 Liu and Curry 1992, Kummerow and Giglio 1994, Petty 1994, Ferraro and Marks 1995,
38 Kummerow et al. 1996, 2001, 2015, Kubota et al. 2007, Gopalan et al. 2010, Mugnai et al.
39 2013, Ebtehaj et al. 2015, Kidd et al. 2016, Petkovic et al. 2018]. The TRMM (Tropical Rainfall
40 Measuring Mission) [Kummerow et al. 2000] and GPM (Global Precipitation Measurement)
41 [Hou et al. 2014, Skofronick-Jackson et al. 2017] satellite missions in particular provided the
42 data and the research framework allowing the successful development of research and
43 operational retrieval algorithms. Today, the GPM Microwave Imager (GMI) is integrated in an
44 international constellation of orbiting imagers providing frequent observations of clouds and
45 precipitation all over the globe [Skofronick-Jackson et al. 2018].

46 The passive microwave retrieval of precipitation relies on the measurement of radiances
47 at the top of the atmosphere, which are the product of the surface emission, emission and

48 absorption by liquid rain drops and water vapor and scattering by ice particles. Vertically and
49 horizontally polarized radiances are measured at various frequencies between 5 and 200 GHz
50 and converted into brightness temperatures (TBs) for physical interpretation. The physical
51 principles of the radiative transfer of microwaves in the atmosphere are well understood and
52 generally accurately reproduced by numerical models. However, the conversion of observed
53 microwave multispectral signatures into hydrometeor profiles (inverse problem) remains
54 uncertain. This uncertainty derives mostly from the inherent underdetermined nature of the
55 inverse problem, that is, while any given hydrometeor profile has a unique spectral signature
56 (assuming known surface emissivity) the inverse is not true [Bauer et al. 2001, Löhnert et al.
57 2001, Sanò et al. 2013, Ebtehaj et al. 2015]. The increasing number of available channels (up
58 to 13 and 14 channels respectively for GMI and AMSR-2 which are the most recent radiometers
59 sent into orbit) allows a better constraining of the inversion, but non-negligible uncertainty still
60 affects the state-of-the-art retrievals.

61 Many algorithms, among which the NASA operational algorithm GPROF [Kummerow
62 et al. 2015], rely on an a-priori database (or dictionary) for the retrieval. The a-priori database
63 is made of a large number of hydrometeor profiles, each one associated with a spectral
64 signature, i.e. a vector of brightness temperatures (TB). The database is typically obtained from
65 actual radiometric measurements collocated with radar observations, or generated using a
66 radiative transfer model to simulate brightness temperatures from the radar-observed
67 hydrometeor profiles. The retrieval generally relies on the computation of radiometric distances
68 (vectorial distances) between the observed TB vector and the TB vectors of the a-priori database
69 to find one or several hydrometeor profiles with a spectral signature close to the observation
70 (called the “neighbors”). An important element in the development of distance-based retrieval
71 algorithms is the choice of the distance metric [Hastie et al. 2009, Petty and Li 2013, Ebtehaj
72 et al. 2015]. In addition to the neighbor search algorithms relying on radiometric distances,

73 some experimental algorithms implement different statistical learning approaches such as
74 neural networks using the same a-priori databases for the training [Tsintikidis et al. 1997, Sanò
75 et al. 2015].

76 The database can be seen as an ensemble of points in the N -dimensional radiometric
77 space (N being the length of the TB vectors, i.e. the number of channels of the imager) where
78 the hydrometeor profile and the surface precipitation rate R are defined. Therefore, for each
79 new radiometric observation, the retrieval of the surface precipitation can be seen as an
80 interpolation problem. However, because different hydrometeor profiles may have very similar
81 or identical spectral signatures (Figures 1a and 1b), the function $R(\mathbf{TB})$ to interpolate is not
82 regular (in the Lipchitz sense) meaning that $\|\mathbf{TB}_i - \mathbf{TB}_j\| \rightarrow 0$ does not necessarily imply that
83 $|R(\mathbf{TB}_i) - R(\mathbf{TB}_j)| \rightarrow 0$ (Figure 1c). Therefore, even with a densely populated database,
84 associating a radiometric observation to the hydrometeor profile of the database having the
85 closest spectral signature may lead to substantial retrieval errors. For this reason, most retrieval
86 algorithms provide smooth estimates of the surface precipitation rate by averaging or combining
87 several profiles of the database having similar spectral signatures instead of associating the
88 observed TB vector to a single hydrometeor profile. Bayesian versions of the retrieval,
89 computing the a-posteriori probability distribution of the precipitation rate given the
90 observations, have also been developed to overcome the uncertainty issue [e.g., Evans et al.
91 1995, Kummerow et al. 2006, Chiu and Petty 2006]. Under the Bayesian framework, one can
92 retain the precipitation rate for which the a-posteriori probability is maximal as the “best”
93 estimate (maximum likelihood estimate). Alternatively, the expected value of the a-posteriori
94 distribution of R is the estimate that theoretically minimizes the mean squared error of the
95 retrieval (minimum mean squared error estimator). Either way, these Bayesian smooth
96 estimators tend to lessen the spatial and temporal variability of precipitation, with mitigation of
97 the extreme values and the statistical distribution of the estimates having a lower variance than

98 the true precipitation fields (provided that the a-priori distribution of the precipitation rates is
99 unimodal, with finite mean and variance) [DeGroot 2004, Foufoula-Georgiou et al. 2014].

100 As already stated, a large part of the final uncertainty on the retrieval is inherent to the
101 incompleteness of the information provided by the vector of observed TBs. When computing
102 the variograms of $R(\mathbf{TB})$ in the TB space, this inherent uncertainty appears as a nugget effect
103 [Cressie 1993] (Figure 1c) and therefore, it cannot be reduced by increasing the density of the
104 retrieval database (or by increasing the size of the training dataset for deep learning algorithms).
105 It is also independent of the distance metric used to compute the distances between the TB
106 vectors. The only way to reduce this uncertainty is to add supplementary information to the
107 vector of observed TBs. This may be achieved by using ancillary datasets, as for example
108 environmental variables from reanalyses [Ferraro et al. 2005, Ringerud et al. 2015, Kidd et al.
109 2016, Petkovic et al. 2018, Taktiri et al. 2019].

110 While the current state-of-the-art algorithms may rely on ancillary data to contextualize
111 the observed TB vectors, they do not use the context information provided by the TB fields
112 themselves. Indeed, the retrieval is performed one pixel at a time and independently for all
113 pixels; that is, each pixel is retrieved only from the TBs measured at the corresponding location
114 and all the neighboring TBs are ignored. Some algorithms have used statistical indices
115 computed over a restrained neighborhood around the pixel of interest to identify cloud type and
116 precipitation type. For example, Prabhakara et al. (2000), and later Gopalan et al. (2010), used
117 the minimum value and the standard deviation of the TB at 85 GHz within a 40 km
118 neighborhood to estimate the convection fraction at the pixel of interest. However, these indices
119 have only been used for unispectral or bispectral algorithms within a linear regression
120 framework so far. What is proposed here is to exploit the information contained in the observed
121 fields of TB by analyzing spatial variations, covariations and patterns of TBs at various scales
122 instead of associating a TB signature to a hydrometeor profile at the “pixel” level as is

123 classically done. Several elements related to the observation geometry and the scale dependence
124 of the relations between precipitation and TBs motivate our resolve to overcome the pixel-wise
125 approach of the retrieval by developing a new “nonlocal” approach. These elements are detailed
126 and supported by examples in this article. The article is organized as follows: Section 2 is
127 dedicated to the description of the used data, namely brightness temperatures from the GMI
128 instrument collocated with observations from the Dual-frequency Precipitation Radar (DPR)
129 onboard the GPM Core Observatory satellite. In section 3, the observation geometry of GMI
130 and other similar passive microwave imagers is described, with particular focus on how this
131 geometry interacts with the three-dimensional structure of precipitation, making the pixel and
132 the resolution of the retrieval not trivial to define. In section 4, relations between measured TBs
133 and precipitation are analyzed in terms of their spatial patterns and scale-dependence.
134 Preliminary results on the reduction of the retrieval uncertainty allowed by using nonlocal
135 information, namely spatial derivatives (gradients) and spatial averages of TBs at various
136 scales, are presented in section 5, while conclusions and perspectives are discussed in section
137 6.

138

139 **2. Data**

140 The analysis presented in this article relies on the brightness temperatures measured by
141 the GPM Microwave Imager (GMI) onboard the Global Precipitation Measurement (GPM)
142 Core Observatory satellite collocated with the measurements from the Dual-Frequency
143 Precipitation Radar (DPR) also onboard the GPM Core Observatory.

144

145 *GMI brightness temperature*

146 The GMI instrument onboard the GPM Core Observatory [Draper et al. 2015] measures
147 the radiances originating from the atmosphere and the Earth's surface below the satellite.
148 Vertically polarized radiances are measured at 10.6, 18.7, 23.8, 37, 89 and 166 GHz (single-
149 band channels), and at 183 ± 3 GHz and 183 ± 7 GHz (double-sideband channels). Horizontally
150 polarized radiances are measured at 10.6, 18.7, 37, 89 and 166 GHz (single-band channels). In
151 the following, the notation 37V designates the 37 GHz vertically polarized channel, the notation
152 89H designates the 89 GHz horizontally polarized channel, etc. The GMI scan is conical with
153 a constant 53° Earth Incidence angle covering an approximately 850-km wide swath. More
154 details on GMI's observation geometry and on its consequence on the retrieval of precipitation
155 are given in section 3. The GPM Core Observatory performs 16 orbits per day covering latitudes
156 between 0° and $\pm 65^\circ$. Its orbit is non sun-synchronous, so the local time of the overpasses is
157 variable. In this article, the brightness temperatures derived from the radiances measured by the
158 13 channels of GMI distributed by NASA under the GPM_1CGPMGMI_R.05 product (GPM
159 GMI Common Calibrated Brightness Temperatures Collocated L1C version 5) are used [Berg
160 2016].

161

162 *DPR reflectivity and near-surface precipitation rate*

163 The DPR instrument is made of two radars operating at 13.6 GHz (Ku band) and 35.5
164 GHz (Ka band). For the statistical analyses performed in this article, only the reflectivities and
165 precipitation rates from the Ku-band Precipitation Radar (KuPR) are used. The KuPR cross-
166 track scan covers 245 km wide swath embedded within the wider swath of GMI. The radar
167 produces three-dimensional reflectivity profiles of the atmosphere below 22 km altitude with a
168 250 m vertical resolution and a 5 km horizontal resolution. The minimum reflectivity
169 measurable by the KuPR is 12 dBZ. In this article, attenuation-corrected reflectivities and radar-
170 derived near-surface precipitation rates from the GPM_2AKu.06 product (GPM DPR Ku

171 Precipitation Profile 2A version 6) [Iguchi and Meneghini 2016a] are used. Ka and Ku/Ka
172 combined precipitation estimates are not used in the present study because the narrower swath
173 of the KaPR (120 km) limits the number of profiles that can be collocated with GMI
174 observations and the extent over which spatial patterns analysis can be performed.

175

176 *GPROF passive-microwave-derived near surface precipitation rate*

177 GPROF is the operational NASA Precipitation Profiling algorithm for the passive
178 microwave imagers of the GPM constellation [Kummerow et al. 2015]. The GPROF version 5
179 near-surface precipitation rate estimates from the GMI instrument
180 (GPM_2AGPROFGPMGMI.05 product) [Iguchi and Meneghini 2016b] are used in this article
181 as reference state-of-the-art passive microwave estimates. The surface classes defined by Aires
182 et al. (2011) and the 2-meter temperature from the ECMWF re-analysis (ERA-interim) used as
183 input of the GPROF algorithm are also used for the analyses presented in this study; these two
184 variables are provided as ancillary data in the GPM_2AGPROFGPMGMI.05 product files.

185

186 **3. Observation geometry and definition of the retrieval pixel**

187 We describe below the observation geometry of the GPM passive Microwave Imager
188 (GMI) onboard the GPM Core Observatory satellite. GMI continuously measures the radiations
189 coming from the surface and the atmosphere below the GPM Core Observatory satellite. For
190 the 9 lower-frequency channels (between 10 and 90 GHz) the mechanical rotation of GMI
191 allows to perform a conical scan at a constant 53° Earth incidence angle over an around 850-
192 km wide swath every 1.9 seconds. Each scan is made of 221 samples, 5 km apart. The distance
193 between two consecutive scans (along-track) is 13.5 km. Each sample corresponds to a different
194 position of the observation beam (or field of view) for each one of the 9 channels. While all 9

195 beams are concentric for a given sample, the beamwidth varies with the frequency; the footprint,
196 defined as the intersection of the -3 dB beam contour with the surface is then different for each
197 channel (Figure 2). The 4 higher-frequency channels of GMI have a slightly different scanning
198 geometry compared to the lower frequencies, with beams centered at different locations [Draper
199 et al. 2015]. In the GPM_1CGPMGMI_R.05 product used in this article, the measured TBs at
200 166 and 183 GHz are interpolated at the locations of the low-frequency observations.

201 The state-of-the-art algorithms perform the retrieval of the local precipitation rate at the
202 intersection of the beams with the surface for each individual sample from the 13 measured
203 TBs. One must note that the fact that each channel has its own footprint creates an issue for the
204 definition of the pixel and resolution of the retrieval. Some retrieval products (arbitrarily) assign
205 the retrieval pixel to the footprint of one of the channels or to an average footprint
206 compromising between the different channel footprints [Munchak and Skofronick-Jackson,
207 2013]. A computational footprint matching method relying on convolution and deconvolution
208 operators has been proposed by Petty and Bennartz (2017) to generate synthetic footprints
209 converging toward the 18.7 GHz footprint for all GMI channels. While the method performs
210 reasonably well for the 23.8 and 37 GHz channels, it is less satisfactory for the 10.6 and 89
211 GHz channels.

212 One shall also consider the fact that for a given channel, the gain of the receiving antenna
213 (i.e. the sensitivity of the imager) is not constant inside the footprint. While the footprints are
214 classically defined as the intersection of the surface with the -3 dB contour of the antenna beam
215 this definition is also partially arbitrary; the -6 dB contour is sometimes used as an alternative
216 for defining radiometric footprints [e.g. Cracknell 1992, Kucera et al. 2004], (for a Gaussian
217 beam 75% of the transmitted/received power is focused inside the -3dB contour and 90% inside
218 the -6dB contour). Regardless of the definition of the retrieval pixel, the assumption that the
219 measured TBs respond to the average precipitation rate inside this pixel is always a very crude

approximation. In the end, when establishing statistical relationships between measured TBs and precipitation rates or constructing a-priori databases for precipitation retrieval, the resolution at which the rain rates are computed is at the discretion of the algorithm developers.

While the target variable of the retrieval is generally the precipitation rate at the surface, the observed TBs are sensitive to the presence of hydrometeors at any altitude in the atmospheric column [Bauer et al. 1998, Fu and Liu 2001, You et al. 2015, Guilloteau et al. 2018]. In fact, in addition to the surface precipitation rate, various parameters characterizing the observed atmospheric column (e.g. integrated liquid/ice water content, precipitation top height, etc.) can be retrieved from the passive microwave TBs [Bauer and Schluessel 1993, Ferraro et al. 2005, Tapiador et al. 2018]. One must note that with the 53° Earth incidence angle of GMI, the observed atmospheric volume for each individual sample is not a vertical but rather a tilted column, which may lead to very heterogeneous and seemingly inconsistent distribution of the hydrometeors inside the observed volume. This is also prone to create a dependence of the measured TBs on the azimuthal direction of the observation [Bauer et al. 1998, Hong et al. 2000]. The consequence of this is that two systems with different spatial structure and different precipitation rates observed from different directions may give rise to similar measured TBs. Additionally, with such a geometry, at a given frequency, a given vertical atmospheric column is always intercepted by several beams at various altitude levels (Figure 3a). Moreover, with different channels responding to the presence of hydrometeors at different altitude levels, the multispectral signature characterizing a given vertical column may be split across several samples. In particular, the signature of the atmospheric ice is likely to appear in beams intercepting the column at a high altitude rather than in the beam intercepting the column at the ground level; this effect is called parallax shift and is documented in several publications [Bauer et al. 1998, Guilloteau et al. 2018]. Additionally, significant overlapping of adjacent fields of

244 view occurs for frequencies lower than 40 GHz. For GMI, at 10.6 GHz, a given atmospheric
245 column may be intercepted by up to 12 different beams (Figure 3b).

246 From these geometrical considerations, neighboring TBs are expected to contain
247 information complementary to that of the local TBs and potentially useful for retrieving
248 precipitation in the pixel of interest. Actually, for the high-frequency channels responding to
249 ice particles at high altitude, because of the parallax shift caused by the 53° Earth incidence
250 angle of the scan, the TBs measured in one or several neighbor pixels are potentially more
251 informative than the local TB for the retrieval of the local precipitation rate [Guilloteau et al.
252 2018]. More generally, with the high incidence angle of the observations, the three-dimensional
253 variability of precipitation systems, including their vertical variability is likely to be partially
254 reflected in the variations of the two-dimensional fields of observed TB. We note that the
255 considerations made here about GMI are also valid for other conical-scanning microwave
256 imagers such as SSMI/S onboard the DMSP satellite series [Kunkee et al. 2008] or AMSR-2
257 onboard the GCOM-W1 satellite [Imaoka et al. 2012] which also have an Earth incidence angle
258 of around 53°, frequency-dependent beamwidths and overlapping fields of view.

259

260 **4. Pattern signature and scale-dependence of the TB-precipitation relations**

261 Because of the observation geometry and instrumental characteristics mentioned in the
262 previous section, the pixel size and spatial resolution of the retrieval of the surface precipitation
263 rate are partially arbitrarily defined (see Guilloteau et al. 2017 for a detailed discussion on the
264 resolution and “effective resolution” of passive microwave retrievals.). Additionally, pixel-wise
265 relations between TBs and precipitation are limited in the sense that they do not account for the
266 fact that precipitation fields are spatially organized at several scales and that the response of the
267 TBs to the spatial variability of precipitation is complex and scale-dependent. Moreover, while

268 some spectral signatures can be ambiguous at the pixel level, the analysis of the spatial patterns
269 of the TBs may allow to partially resolve this ambiguity. In other words, some specific
270 atmospheric features are expected to generate specific spatial patterns (or geometric signatures)
271 rendering them more easily identifiable in the TB fields. We present here two case studies
272 illustrating this fact.

273 The first case study is identified through the analysis of a database of 4 million GPM
274 KuPR radar reflectivity profiles and near-surface precipitation rates over ocean, associated to
275 collocated GMI TB vectors at the pixel level. One of the reflectivity profiles of this database,
276 showing a 149 mm/h precipitation rate at the surface (average rate in the 18.7 GHz GMI -3 dB
277 footprint) is associated to a 278 K brightness temperature at 89 GHz (vertical polarization).
278 Such a high TB at 89 GHz indicates that the observed atmospheric column contains no (or few)
279 ice particles. The absence of a significant amount of ice is very surprising as liquid-phase only
280 precipitation processes are unlikely to generate instantaneous precipitation rates higher than 50
281 mm/h [Liu and Zipser 2009, Lebsack and L'Ecuyer 2011]. In fact, precipitation rates as high
282 as 149 mm/h are expected to be associated with convective systems showing radar echo tops
283 several kilometers above the melting layer [Tokay et al. 1999, Hamada et al. 2015]. This
284 particular profile was observed over the South China Sea at latitude 22.1° and longitude 17.7°
285 on 2016-10-09 at 04:45 UTC (orbit #14851 of the GPM Core observatory). Figure 4 shows the
286 GMI-observed fields of TB at 10.6, 37 and 89 GHz (vertical polarization) in the vicinity of this
287 profile, as well as the near-surface precipitation fields derived from the TBs using the NASA
288 operational algorithm GPROF and the near-surface precipitation derived from the DPR. The
289 above-mentioned profile is located near the southeastern edge of a 60km by 30km area with
290 extremely intense radar near-surface precipitation rates (higher than 60 mm/h and locally higher
291 than 200 mm/h). The high TBs (between 225 and 260 K) measured by GMI at 10.6 GHz inside

292 this area, indicating strong emission from liquid rain drops, are consistent with the radar
293 observations.

294 We noticed previously the absence of ice scattering signature at 89 GHz in a pixel where
295 the DPR-estimated surface precipitation rate is 149 mm/h. In fact, a 180-K depression caused
296 by the ice scattering actually appears in the 89 GHz TB field, about 40 km North West from the
297 location of maximum DPR near-surface precipitation rate. It is interesting to note that the
298 location of the maximum of the 89 GHz TB depression corresponds to a non-precipitation area
299 according to the DPR. The analysis of the three-dimensional structure of the precipitation
300 system seen by the DPR reveals a deep convective system with an echo top above 15 km altitude
301 (Figure 5). It can be seen that the maximum of the radar reflectivity above 10 km altitude is
302 horizontally shifted by about 20 km relatively to the location of the maximum near-surface
303 reflectivity because the system has a tilted vertical structure. Additionally, the parallax effect,
304 caused by the Earth incidence angle of the passive microwave imager associated with the fact
305 that the 89 GHz TB responds primarily to the presence of ice in the upper layer of the clouds
306 generates a shift between the apparent location of the ice-scattering signature at 89 GHz and
307 the actual location of the ice clusters. This shift is proportional to the mean altitude of the center
308 of gravity of the ice [Bauer et al. 1998, Guilloteau et al. 2018]. In the present case study, the
309 parallax shift is of the order of 15 to 20 km and adds to the physical horizontal shift between
310 the high-altitude ice cluster and the maximum of the near-surface precipitation. Hong et al.
311 (2000) also analyzed tilted convective systems observed by aircraft and ground-based radars
312 and space-borne microwave imagers (TMI and SSMI) and reported shifts up to 100 km between
313 the maximum of the liquid emission signal and the maximum of the ice scattering signal.

314 The estimated precipitation field derived from the passive microwave observations with
315 the GPROF algorithm shows a correct location of the precipitation at the surface but also a
316 severe underestimation of the precipitation rate. The GPROF algorithm successfully associates

317 the emission signal at 10 to 40 GHz with the precipitating area, but, with the absence of a
318 significant ice scattering signal in the corresponding pixels, it fails to identify the extremely
319 active deep convective cell. The geometric mismatch between the emission signal and the
320 scattering signal therefore penalizes the retrieval. Nevertheless, the observed spatial shift
321 between the liquid emission signal at 10.6 GHz and the ice-scattering signal at 89 GHz
322 potentially provides information about the underlying structure of the observed precipitation
323 system, revealing in particular its vertical development; however, an algorithm relying on pixel-
324 wise relations between TB and precipitation cannot leverage this information.

325 The interpretation of the spatial patterns of the brightness temperature can be
326 particularly informative for channels that are sensitive to both ice scattering and liquid emission.
327 This is the case in particular for the 37 GHz channels of GMI. In the present case study, the
328 combination of the ice scattering and liquid emission signals generates a strong TB gradient at
329 37 GHz between the area where the emission signal is dominant and the area where the
330 scattering signal is dominant (Figure 4). Because of the 53° Earth incidence angle of GMI, this
331 gradient reveals both the horizontal and vertical structure of the precipitation system. One must
332 note that, because the area where the surface precipitation is the most intense is located at the
333 limit between the areas of strong ice scattering and strong liquid emission, it shows moderately
334 high TBs at 37 GHz, similar to those observed in areas with low precipitation rates. One can
335 also note that the shift between the maximum of the ice scattering signal and the maximum of
336 the surface precipitation rate is smaller at 37 GHz than at 89 GHz, which can be explained by
337 the fact that the 37 GHz channel is sensitive to larger ice particles found at lower altitudes.

338 The second case study illustrates more specifically the particularity of the 37 GHz
339 channels, which are sensitive to both liquid raindrops emission and ice scattering. (One must
340 note that all channels are potentially sensitive to both phenomena, however the emission signal
341 is generally dominant for frequencies lower than 30 GHz and the scattering signal is dominant

for frequencies higher than 50 GHz [Liu and Curry, 1992]). Because of this, the 37 GHz TBs have a non-monotonic response to the intensity of precipitation [Spencer 1986]: the absence of precipitation is associated with medium TBs, low or medium precipitation rates are associated with high TBs, high convective precipitation rates are associated with medium TBs and extreme deep convective precipitation rates are associated with low TBs. Figure 6 shows a tropical mesoscale convective system observed by GMI at 37 GHz and 89 GHz over the Atlantic Ocean off the coast of Brazil on 2016-10-09 at 06:40 UTC (orbit #14852). At 37 GHz the system appears as a 300 km by 300 km area with an average TB higher than 245 K (while the TB of the ocean in the surrounding precipitation-free area is around 230 K). Strong variations of the 37 GHz TB can be observed within the system with TBs locally higher than 275 K and several areas of low or medium TBs (230 to 250 K) embedded inside a larger region with relatively high mean TB. A strong depression of the 37 GHz TB can be observed at the South-Eastern edge of the system, reaching a minimum value lower than 200 K. At 89 GHz, identifying the extent of the precipitating area is uneasy, but one can observe depressions of the TB caused by ice scattering at several locations coinciding with local minima of the 37 GHz TB. This indicates that the variations of the 37 GHz TB inside the system are mostly caused by the ice scattering rather than resulting from variations of the liquid rain drops emission signal.

From this last case study, it seems that while the coarse-scale variations of the 37 GHz TB (i.e. spatial averages over large areas) are dominated by the liquid drops emission signal, fine-scale local variations (intra-system variability) is dominated by the ice-scattering signal. Statistics at the global scale confirm this finding. The coefficient of linear correlation between the 37V and 89V TBs computed from 4 years of GMI measurements over ocean (see Figure 7a) is -0.08 (excluding non-precipitating areas). Both TBs are corrected from the influence of the surface temperature (assimilated to the ERA-Interim 2-m temperature), assuming a linear relation between TB and surface temperature (see appendix B and Guilloteau et al. 2018 for

367 more details). While from the previous result the 37 GHz and 89 GHz TBs do not appear to be
368 linearly correlated, after removing the fine-scale spatial variations in both TB fields through
369 low-pass filtering (convolution with a Gaussian smoothing kernel, with $\sigma = 30$ km) we find a -
370 0.47 correlation coefficient between the two TBs (Figure 7b). On the contrary, if we apply a
371 high-pass filtering (isotropic Laplacian of Gaussian differentiating kernel, with $\sigma = 15$ km), we
372 find a positive 0.24 correlation between the two TBs (Figure 7c). Assuming that the 89 GHz
373 TB responds essentially to ice scattering at all scales, this confirms that the fine-scale variability
374 of the 37 GHz TB in precipitating areas is dominated by the ice-scattering signal, while the
375 coarse-scale variability is dominated by the liquid rain drops emission signal. Once again, this
376 illustrates the complexity of the scale-dependent relations between the TBs and precipitation,
377 which if understood and quantified can be leveraged for improved retrieval.

378 While inferring a precipitation regime and precipitation rate from the pixel value of the
379 37 GHz TB may not always be possible because of the ambiguous non-monotonic relation
380 between the two variables, the analysis of the spatial pattern of the 37 GHz TB field can help
381 resolve the ambiguity. For example, an area of medium or low TBs embedded inside an area of
382 high TBs is a typical pattern signature of a deep convective cell, generally associated with high
383 precipitation rates. Convective cells are also prone to appear as dipoles in the 37 GHz TB fields,
384 with a local maximum caused by liquid emission close to a local minimum caused by ice
385 scattering. Even if the system is not tilted, the emission and scattering signals may be spatially
386 shifted because of the incidence angle of the microwave imager. This may be beneficial for
387 retrieval as it prevents the scattering and emission signals at 37 GHz from cancelling each other
388 out.

389

390 **5. Extracting nonlocal parameters for enriched radiometric information and reduced**
391 **retrieval uncertainty**

392 The results presented in the previous section show that the spatial patterns of the TBs
393 potentially contain useful information for retrieving hydrometeor profiles and estimating the
394 surface precipitation rate. Convolution filters are a widely used potent tool for the analysis of
395 the spatial variations and patterns in images or physical fields [Milligan and Gunn 1997,
396 Szeliski 2010]. For numerical images, the filtering operation simply consists of convolving the
397 image with a convolution matrix (or kernel). Various standardized types of kernels exist,
398 enabling blurring, smoothing and sharpening, as well as edge and pattern extraction with or
399 without dependence on directionality. Some families of convolution kernels such as wavelets,
400 designed for multiresolution analysis [Kumar and Foufoula-Georgiou 1997] are potentially
401 useful for analyzing and utilizing the scale-dependent relations between TBs and precipitation
402 [Turiel et al. 2005, Guilloteau et al. 2017, Klein et al. 2018]. We call a “nonlocal radiometric
403 parameter” the result of the convolution of the TB field with a predefined kernel at a given
404 location. For each pixel and for each radiometric channel many different nonlocal parameters
405 can be computed using different convolution kernels. Including these nonlocal parameters in
406 the a-priori database allows for a more comprehensive radiometric characterization of each
407 individual hydrometeor profile of the database.

408 For algorithms relying on the computation of the radiometric distance between the
409 observation and the profiles of the a-priori database, the nonlocal parameters can then be used
410 to form enriched radiometric vectors and compute the radiometric distances in a higher-
411 dimensional space. This is expected to partially resolve the ambiguity between radiometric
412 signatures and hydrometeor profiles, allowing to distinguish previously indistinguishable
413 hydrometeor profiles from the enriched radiometric information. While many different nonlocal
414 radiometric parameters can potentially be computed, a parsimonious parametrization is always
415 preferable for computational efficiency. Moreover, for a retrieval based on radiometric distance,
416 it is also preferable to keep the number of dimensions of the radiometric space low enough to

417 ensure that the radiometric vectors of the database stay reasonably close to each other [Beyer
418 et al. 1999].

419 As a proof of concept, a simple k -nearest neighbors retrieval algorithm [Hastie et al.
420 2009] has been implemented using two 700,000-member a-priori databases of DPR
421 hydrometeor profiles associated with collocated GMI radiometric measurements. The first
422 database contains only profiles over vegetated land surfaces, excluding in particular coastal
423 areas and snow-covered areas. For this, we rely on the surface type classification used in the
424 current operational implementation (V05) of the GPROF algorithm [Aires et al. (2011)]. The
425 vegetated surface classes account for 70% of all land surfaces at the latitudes covered by the
426 GPM core observatory. The second database contains only profiles over ocean. Each profile of
427 the two databases is associated with the 13 TBs between 10 and 183 GHz measured by GMI,
428 the 2-m temperature derived from the ERA-interim reanalysis, and 3 nonlocal radiometric
429 parameters. The k -nearest neighbors search is therefore performed in a 17-dimensional space.

430 The first two nonlocal parameters are chosen to characterize the spatial derivative of the
431 37V and 89V TBs in the azimuthal direction of GMI's observation beam. These two parameters
432 are obtained by convolving the 37V and 89V TB fields with a first derivative of Gaussian kernel
433 (with $\sigma = 8$ km, Figure 8a). Figure 9 (a and b) shows that, over land, the statistical relations
434 between surface precipitation rate and the local value of the 37V and 89V TBs vary significantly
435 when conditioned on the value of the two nonlocal parameters; in particular, they vary
436 depending on the sign of these two parameters. For example, when the spatial derivative of the
437 89V TB in the azimuthal direction of the beam is negative, the precipitation rate is on average
438 2.4 times higher than when the derivative is positive (while the conditional marginal distribution
439 of the local 89V TB is identical for the two cases). A similar result is found with the spatial
440 derivative of the 37V TB. This asymmetry is the consequence of the tilted observation beam of
441 GMI as illustrated in Figure 9c. In fact, the 37V and 89V TB gradients partially reflect the

442 vertical variability of the precipitating system. The most intense precipitation rates are more
443 likely to be found in the areas where the gradient is negative, i.e., when a lower 37V and / or
444 89V TB is measured in the next field of view in the azimuthal direction of the observation
445 (which intercepts the same atmospheric column 10 km higher), as this is likely to indicate the
446 presence of ice particles at high altitude. Including the 37V and 89V directional gradients in the
447 retrieval scheme is expected to help differentiating precipitating systems which have different
448 three-dimensional structure but show similar spectral signatures when observed from different
449 azimuthal angles. It is also expected to allow identifying profiles which are potentially affected
450 by the parallax shift effect.

451 The third parameter is obtained by convolving the 37 V TB field with a Gaussian low-
452 pass filtering kernel (with $\sigma = 20$ km, Figure 8b). This parameter is expected to characterize the
453 liquid rain emission signal at 37 GHz by removing the fine-scale spatial variations associated
454 with the ice scattering (Figure 8d); consequently, the difference between this parameter and the
455 raw 37 GHz TB is expected to characterize the ice-scattering signal only.

456 The target variable of the k -nearest neighbors retrieval is the average near-surface
457 precipitation rate inside the 18.7 GHz -3 dB footprint of GMI. For each new radiometric
458 observation over land or over ocean, the radiometric distance to each profile of the
459 corresponding database is computed as a Euclidean distance:

460
$$D_{o,i} = \|\mathbf{V}_i - \mathbf{V}_o\|$$

461 \mathbf{V}_o , belonging to \mathbb{R}^{17} , is the observed radiometric vector made of the 13 GMI TBs (pixel
462 values), plus the 2-m temperature and the 3 nonlocal radiometric parameters. \mathbf{V}_i , belonging to
463 \mathbb{R}^{17} , is the corresponding radiometric vector associated with the i^{th} profile of the a-priori
464 database (with i belonging to $\{1, 2 \dots, 7 \times 10^5\}$). The k profiles of the database for which $D_{o,i}$
465 is minimal are retained and the final estimate of the near-surface precipitation rate R_{GMI} is

simply the mean value (without weighting) of the k near-surface radar-derived precipitation rates R_{DPR} associated to these k profiles. This extremely simple retrieval scheme is used to demonstrate that the nonlocal parameters contain information useful to reduce the retrieval uncertainty. The use of nonlocal parameters in a neighbor-search algorithm does not require defining explicit relations between TB patterns and precipitation; it is simply assumed that similar TB patterns correspond to similar precipitation systems and geometries. In particular, with this approach, it is not necessary to explicitly correct for the parallax shift as is done in Guilloteau et al. (2018).

The retrieval performance is evaluated over 6 million randomly sampled DPR profiles and collocated GMI TBs (3 million profiles over ocean and 3 million profiles over land, all independent from those of the retrieval databases), with k varying between 1 and 28. For comparison, the retrieval is also performed without including the nonlocal parameters in the vectors \mathbf{V}_o and \mathbf{V}_i , thus computing the radiometric distances $D_{o,i}$ in a 14-dimensional space (13 GMI TBs plus the 2-m temperature). Figure 10 (top) shows the mean absolute retrieval error (mean absolute difference between the GMI-retrieved precipitation rate and the DPR Ku precipitation rate $E[|R_{GMI} - R_{DPR}|]$ with $| \cdot |$ denoting the absolute value) as a function of k with and without using the nonlocal parameters. One can see that, for all values of k , the inclusion of the three nonlocal parameters allows a reduction of the mean absolute error of around 11% over land and around 6% over ocean. Additionally, it can be seen that the same level of mean absolute error can be reached with a smaller value of k , i.e. a less smooth estimate for the retrieval using the nonlocal information. For k greater than 15, the mean absolute error is found stable around 0.195 mm/h over land and around 0.124 mm/h over ocean. For comparison, the mean absolute errors for the GPROF estimates on the same test datasets are respectively 0.266 mm/h and 0.154 mm/h.

490 The ability of non-local parameters to help the k -nearest neighbors algorithm
491 distinguishing between precipitating and non-precipitating profiles is also tested. The observed
492 scene is considered precipitating if the majority of the k profiles of the retrieval database
493 selected by the k -nearest neighbors algorithm are associated to a non-zero surface precipitation
494 rates (with a 0.3 mm/h detection threshold). This is implemented only with odd values of k to
495 avoid indecisive results (i.e. 50% of the k profiles being precipitating profiles). Significant
496 improvement of the detection rate (percentage of precipitating profiles correctly identified) is
497 observed over both ocean and land surfaces when including the nonlocal parameters: from 81%
498 to 86% over land and 94% to 95% over ocean (Figure 10, middle). In terms of false detection
499 rate (percentage of profiles classified as precipitating by k -nearest neighbors algorithm which
500 are non-precipitating according to the radar), the improvement is faint over ocean. Over land,
501 when k is higher than 15, the false detection rate is reduced from 3.6% to 2.6% (Figure 10,
502 bottom). This improvement in detection performance can be attributed to a better localization
503 of the edges of the systems allowed by the nonlocal parameters. Considering that the two
504 evaluation datasets are made of 3 million independent profiles, for all the considered scoring
505 metrics (mean retrieval error, detection rate and false detection rate) the improvement is
506 statistically significant at the 99% level.

507 Figure 11 shows that the reduction of the mean absolute error due to incorporation of
508 the nonlocal parameters affects the retrieval of stratiform-type precipitation as well as
509 convective-type precipitation. Precipitation type is determined from the KuPR reflectivity
510 profile using the Awaka et al., 1997, method. A microwave pixel is classified as stratiform
511 (convective) if 60% or more of the 18.7 GHz footprint is classified as stratiform (convective)
512 from the KuPR. All other precipitating profiles are classified as mixed or undetermined
513 precipitation type. While over land the nonlocal parameters allow only very little improvement
514 for stratiform-type precipitation, the reduction of the mean absolute error is noticeable for

515 convective-type precipitation and is particularly salient for mixed / undetermined precipitation
516 type. Over ocean, the improvement is more salient for stratiform and mixed / undetermined
517 precipitation types than for convective precipitation.

518

519 **6. Conclusions and perspectives**

520 The retrieval of surface precipitation from passive microwave observations is
521 intrinsically uncertain to some degree because of the limited information content of the
522 radiometric measurements. In the present article, we illustrate via case studies the fact that the
523 relations between TBs and precipitation constructed at the “pixel” level are limited by the fact
524 that: 1) due to the observation geometry, the multispectral information characterizing the local
525 state of the atmosphere can be spatially shifted and split across several neighboring pixels; 2)
526 the relations between TBs and precipitation can be non-monotonic and scale-dependent. These
527 results motivate a new direction for passive microwave precipitation retrieval that moves away
528 from the pixel-wise only approach and considers the spatial patterns and variations /
529 covariations of TBs at various scales. We call it a “nonlocal retrieval approach” and note that
530 although it is potentially pertinent for the remote sensing of any spatial variable, it is particularly
531 relevant for vertically-integrated atmospheric measurements, as the observed horizontal
532 variability may partially reflect the vertical variability of the underlying process (horizontal and
533 vertical variations being dynamically coupled).

534 From a global analysis over land and ocean, we show that using standard convolution
535 filters (Gaussian and derivative of Gaussian) to extract nonlocal parameters from the TB fields
536 allows to define enriched spectral signatures that can help resolve the ambiguity in the TB-
537 precipitation relations. In particular, at 37 GHz, scale-dependent information extracted through
538 convolution filters enables to partially separate the liquid drops emission signal from the ice

539 scattering signal, the latter being associated with finer scale variations. The nonlocal parameters
540 are also useful in handling the complex observation geometry of conical-scanning microwave
541 imagers. For example, considering the spatial derivative of the ice-sensitive TBs (higher than
542 30 GHz) in the azimuthal direction of the imager's observation beam helps characterizing the
543 vertical variability of hydrometeor profiles and handling the parallax shift effect.

544 Initial results show that adding only three nonlocal parameters to the vector of TBs for
545 the computation of the radiometric distances in a k -nearest neighbors retrieval scheme allows
546 improving the retrieval performance scores over ocean and land surfaces. Over land, the
547 detection rate is improved from 81% to 86%, the false alarm ratio is reduced from 3.6% to 2.6%
548 and the mean absolute error is reduced from 0.212 mm/h to 0.195 mm/h. Over ocean, the
549 detection rate is improved from 94% to 95% and the mean absolute error is reduced from 0.132
550 mm/h to 0.124 mm/h, all improvements being statistically significant. While improvement is
551 noticed for the retrieval of both stratiform and convective type precipitation, the most
552 significant improvement occurs when the precipitation type is not homogeneous within the 18.7
553 GHz footprint or when the precipitation type could not be determined by the radar algorithm,
554 i.e., for atypical profiles, which are known to be challenging for passive microwave
555 precipitation retrievals.

556 The interpretation of the TB fields is always easier over ocean than over land surfaces
557 because of the complex varying background emission of land surfaces. In particular, the surface
558 emissivity makes the interpretation of the low-frequency liquid emission-sensitive TBs notably
559 complicated over land surfaces. Therefore, passive microwave retrieval over land relies
560 preferably on the high-frequency ice-scattering signal. It must be noted that, although the
561 illustrative cases studies presented in section 4 are oceanic systems, the three nonlocal
562 parameters retained for the retrieval demonstration essentially improve the characterization of
563 the ice-scattering signal, allowing a more salient improvement of the retrieval over land surfaces

564 (11% reduction of the mean absolute retrieval error against 6% over ocean). Scale
565 decomposition and pattern extraction may also help distinguishing the atmospheric signal from
566 the background surface signal over land. The addition of more than three nonlocal parameters
567 in the k -nearest neighbors retrieval scheme (not shown) was not found to further improve the
568 retrieval in terms of global statistics; however, this may be due to the limited ability of the k -
569 nearest neighbors algorithm to handle high-dimensional problems. The patterns at 166 and 183
570 GHz in particular are expected to contain information similar to the 89 GHz patterns with
571 potentially higher benefits for the identification of small ice particles and of falling snow. One
572 shall note that the nonlocal parameters used here for the initial demonstration are the same over
573 land and ocean; however, surface-specific fine-tuning and parameter optimization is likely to
574 allow further improvement of the retrieval performance and this is a topic for future research.

575 Apart from the nonlocal parameters extracted with linear convolution filters examined
576 in this study, various methods can also be explored for extracting nonlocal information from
577 the fields of TB and to determine an optimal set of parameters in terms of both parsimony and
578 information content [Hastie et al. 2009]. For example, as an alternative to the heuristic approach
579 used here within a k -nearest neighbors retrieval framework, learning via neural networks, which
580 has already been successfully used for the retrieval of precipitation from passive instruments
581 [Hsu et al. 1997, Hong et al. 2004, Sanò et al. 2015], offers an attractive alternative in terms of
582 extracting pattern information. The results of the present study advocate in particular for the
583 use of deep convolutional neural networks, a class of neural networks using convolution filters
584 [Lecun et al. 2015, Nogueira et al. 2017]. However, a prior comprehensive analysis of the
585 retrieval problem and of the available datasets is always necessary to guide the machine learning
586 approach (for example to help choose the topology of a neural network).

587 One of the arguments for the necessity of overcoming the pixel-wise approach of
588 precipitation retrieval from passive microwave sensors is the spatial shift between the liquid

589 rain drops emission signal and the ice scattering signal. As already noted by Hong et al. (2000),
590 this effect is naturally more salient when the instrumental resolution is higher. Consequently,
591 higher instrumental resolution may paradoxically be disadvantageous for the retrieval of
592 precipitation, and particularly for the retrieval of the fine-scale variability with a pixel-wise
593 retrieval scheme. The nonlocal retrieval approach proposed herein may therefore allow to
594 realize the full benefits of the increased resolution and accuracy of the most recent and future
595 microwave imagers.

596 We presented herein the use of nonlocal parameters to enrich the spectral signatures
597 derived from the conical-scanning passive microwave imager GMI (onboard the GPM Core
598 Observatory satellite) specifically designed for the retrieval of precipitation. It must be noted
599 that precipitation can also be detected and measured from passive microwave imagers designed
600 for other purposes such as the cross-track scanning humidity sounders MHS and SAPHIR [Kidd
601 et al. 2016]. Because these instruments have fewer channels than GMI, in particular they miss
602 the low-frequency channels sensitive to liquid drops emission and the polarization information,
603 the (pixel-wise) spectral signatures they produce have a poorer information content regarding
604 precipitation. Therefore, the incremental gain of using nonlocal parameters to retrieve
605 precipitation from these types of instruments is potentially higher than for the conical-scanning
606 microwave imagers such as GMI, SSMI-S and AMSR-2. One must note that multisensor
607 precipitation products such as CMORPH [Xie et al 2017], IMERG [Huffman et al. 2018] or
608 GSMP-MVK [Ushio et al. 2009], providing global mapping of hourly or half-hourly
609 cumulative precipitation, rely on instantaneous precipitation retrievals from both conical-
610 scanning imagers and cross-track sounders. Thus, exploring the non-local retrieval approach
611 holds great potential for improving the accuracy and space-time resolution of multisensor
612 merged products.

613

614 **Acknowledgments**

615 This work was supported by the NASA Global Precipitation Measurement Program
616 under Grant 80NSSC19K0684 and by NSF grants DMS-1839336 and ECCS-1839441. The
617 authors thank Prof. Christian Kummerow, Dr. Dave Randel and Dr. Wesley Berg from the
618 Precipitation Group at the Colorado State University as well as Dr. Joseph Turk from NASA
619 Jet Propulsion Laboratory for the insightful discussions and shared information which
620 contributed to the present article.

621 **Appendix A: Acronyms**

- 622 AMSR-2: Advanced Microwave Scanning Radiometer #2
- 623 CMORPH: Climate prediction center MORPHing technique
- 624 DMSP: Defense Meteorological Satellite Program
- 625 DPR: Dual-frequency Precipitation Radar
- 626 ECMWF: European Centre for Medium-Range Weather Forecasts
- 627 ERA: ECMWF Re-Analysis
- 628 GCOM-W1: Global Change Observation Mission – Water, satellite #1
- 629 GMI: GPM Microwave Imager
- 630 GPM: Global Precipitation Measurement
- 631 GPROF: Goddard PROFiling algorithm
- 632 GSMAp-MVK: Global Satellite Mapping of Precipitation with Moving Vectors and Kalman
633 filtering
- 634 IMERG: Integrated Multi-satellitE Retrievals for GPM
- 635 KuPR: Ku Precipitation Radar
- 636 MHS: Microwave Humidity Sounder
- 637 NASA: National Aeronautics and Space Administration
- 638 SAPHIR: Sondeur Atmosphérique du Profil d'Humidité Intertropicale (atmospheric sounder
639 for intertropical humidity profile)
- 640 SMMR: Scanning Multichannel Microwave Radiometer

641 SSMI: Special Sensor Microwave Imager
642 SSMI/S: Special Sensor Microwave Imager/Sounder
643 TB: Brightness Temperature
644 TMI: TRMM microwave imager
645 TRMM: Tropical Rainfall Measuring Mission

646

647 **Appendix B: Correcting observed TBs from the influence of the surface temperature.**

648 The method used in Guilloteau et al. (2018) to correct GMI's 89V TBs from the
649 influence of the surface temperature is used here over ocean for the 89V and 37V channels. In
650 non-precipitating areas, two linear regressions are performed between GMI 37V TB and ERA-
651 interim 2-m temperature and between the 89V TB and the 2-m temperature. We establish the
652 following relations between TB_{37V} , TB_{89V} and T_{2m} expressed in Kelvin in non-precipitating
653 areas:

654 $TB_{37V_NP} = 31.15 + 0.595 T_{2m}$ (B.1)

655 and:

656 $TB_{89V_NP} = -117.12 + 1.248 T_{2m}$ (B.2)

657 We define the corrected 37V and 89V TBs as:

658 $TB_{37V_cor} = TB_{37V} - TB_{37V_NP}$ (B.3)

659 and:

660 $TB_{89V_cor} = TB_{89V} - TB_{89V_NP}$ (B.4)

661 The corrected TBs are expected to vary only due to hydrometeors and should have a value
662 close to 0 K for non-precipitating profiles.

663 **References:**

664

665 Aires, F., C. Prigent, F. Bernardo, C. Jiménez, R. Saunders, and P. Brunel, 2011: A Tool to
666 Estimate Land-Surface Emissivities at Microwave frequencies (TELSEM) for use in numerical
667 weather prediction. *Quarterly Journal of the Royal Meteorological Society*, **137**(656), 690-699,
668 doi:10.1002/qj.803.

669

670 Awaka, J., T. Iguchi, H. Kumagai, and K.I. Okamoto, 1997: Rain type classification algorithm
671 for TRMM precipitation radar. *Proceedings of the IEEE International Geoscience and Remote
672 Sensing Symposium*, **4**, 1633-1635, doi:10.1109/IGARSS.1997.608993.

673

674 Bauer, P., and P. Schluessel, 1993: Rainfall, total water, ice water, and water vapor over sea
675 from polarized microwave simulations and Special Sensor Microwave/Imager data. *Journal of
676 Geophysical Research: Atmospheres*, **98**(D11), 20737-20759, doi:10.1029/93JD01577.

677

678 Bauer, P., L. Schanz, and L. Roberti, 1998: Correction of three-dimensional effects for passive
679 microwave remote sensing of convective clouds. *Journal of Applied Meteorology*, **37**(12),
680 1619-1632, doi:10.1175/1520-0450(1998)037<1619:COTDEF>2.0.CO;2

681

682 Bauer, P., P. Amayenc, C.D. Kummerow, and E. A. Smith, 2001: Over-ocean rainfall retrieval
683 from multisensor data of the Tropical Rainfall Measuring Mission. Part II: Algorithm
684 implementation. *Journal of Atmospheric and Oceanic Technology*, **18**(11), 1838-1855,
685 doi:10.1175/1520-0426(2001)018<1838:OORRFM>2.0.CO;2.

686

687 Berg, W., 2016: GPM GMI_R Common Calibrated Brightness Temperatures Collocated L1C
688 1.5 hours 13 km V05. Goddard Earth Sciences Data and Information Services Center (GES
689 DISC), accessed 2019-11-01, doi:10.5067/GPM/GMI/R/1C/05.

690

691 Beyer, K., J. Goldstein, R. Ramakrishnan, and U. Shaft: 1999: When is “nearest neighbor”
692 meaningful?. In *Proceedings of the 7th International conference on database theory*. ed.
693 Springer, 217-235.

694

695 Chiu, J. C., and G. W. Petty, 2006: Bayesian retrieval of complete posterior PDFs of oceanic
696 rain rate from microwave observations. *Journal of applied meteorology and climatology*, **45**(8),
697 1073-1095, doi:10.1175/JAM2392.1

698

699 Cracknell, A. P. (1992). Passive microwave techniques. In *Space Oceanography: An Intensive
700 Course*, ed. World Scientific, 321-354.

701

702 Cressie, N., 1993: Geostatistical data. In *Statistics for spatial data*, ed. Wiley, 21-381.

703

704 DeGroot, M. H., 2004: *Optimal Statistical Decisions*. John Wiley & Sons, 489 pp,
705 doi:10.1002/0471729000.

706

707 Draper, D. W., D. A. Newell, F. J. Wentz, S. Krimchansky, and G. M. Skofronick-Jackson,
708 2015: The global precipitation measurement (GPM) microwave imager (GMI): Instrument
709 overview and early on-orbit performance. *IEEE Journal of Selected Topics in Applied Earth
710 Observations and Remote Sensing*, **8**(7), 3452-3462, doi:10.1109/JSTARS.2015.2403303.

711

712 Ebtehaj, A.M., R. L. Bras, and E. Foufoula-Georgiou, 2015: Shrunken locally linear embedding
713 for passive microwave retrieval of precipitation. *IEEE Transactions on Geoscience and Remote*
714 *Sensing*, **53**(7), 3720-3736, doi:10.1109/TGRS.2014.2382436.

715

716 Evans, K. F., J. Turk, T. Wong, and G. L. Stephens, 1995: A Bayesian approach to microwave
717 precipitation profile retrieval. *Journal of Applied Meteorology*, **34**(1), 260-279,
718 doi:10.1175/1520-0450-34.1.260.

719

720 Ferraro, R. R., and G. F. Marks, 1995: The development of SSM/I rain-rate retrieval algorithms
721 using ground-based radar measurements. *Journal of Atmospheric and Oceanic Technology*,
722 **12**(4), 755-770, doi:10.1175/1520-0426(1995)012<0755:TDOSRR>2.0.CO;2.

723

724 Ferraro, R.R., F. Weng, N. C. Grody, L. Zhao, H. Meng, C. Kongoli, P. Pellegrino, S. Qiu, and
725 C. Dean, 2005: NOAA operational hydrological products derived from the advanced
726 microwave sounding unit. *IEEE Transactions on Geoscience and Remote Sensing*, **43**(5), 1036-
727 1049, doi:10.1109/TGRS.2004.843249.

728

729 Foufoula-Georgiou, E., A. M. Ebtehaj, S. Q. Zhang, and A. Y. Hou, 2014: Downscaling satellite
730 precipitation with emphasis on extremes: A variational ‘1-norm regularization in the derivative
731 domain. *Surv. Geophys.*, **35**, 765–783, doi:10.1007/s10712-013-92649.

732

733 Fu, Y., and G. Liu, 2001: The variability of tropical precipitation profiles and its impact on
734 microwave brightness temperatures as inferred from TRMM data. *Journal of applied*
735 *meteorology*, **40**(12), 2130-2143, doi:10.1175/1520-0450(2001)040<2130:TVOTPP>2.0.CO;2.

736

737 Gopalan, K., N. Y. Wang, R. Ferraro, and C. Liu, 2010: Status of the TRMM 2A12 land
738 precipitation algorithm. *Journal of Atmospheric and Oceanic Technology*, **27**(8), 1343-1354,
739 doi:10.1175/2010JTECHA1454.1.

740

741 Guilloteau, C., E. Foufoula-Georgiou, and C. D. Kummerow, 2017: Global multiscale
742 evaluation of satellite passive microwave retrieval of precipitation during the TRMM and GPM
743 eras: effective resolution and regional diagnostics for future algorithm development. *Journal of*
744 *Hydrometeorology*, **18**(11), 3051-3070, doi:10.1175/JHM-D-17-0087.1.

745

746 Guilloteau, C., E. Foufoula-Georgiou, C. D. Kummerow, and V. Petković, 2018: Resolving
747 surface rain from GMI high-frequency channels: limits imposed by the three-dimensional
748 structure of precipitation. *Journal of Atmospheric and Oceanic Technology*, **35**(9), 1835-1847,
749 doi:10.1175/JTECH-D-18-0011.1.

750

751 Hamada, A., Takayabu, Y.N., Liu, C. and Zipser, E.J., 2015. Weak linkage between the heaviest
752 rainfall and tallest storms. *Nature communications*, **6**, 6213, doi:10.1038/ncomms7213.

753

754 Hastie, T., R. Tibshirani and J. Friedman, 2009: *The elements of statistical learning, data*
755 *mining, inference, and prediction, second edition*. ed. Springer, 745 pp, doi: 10.1007/978-0-
756 387-84858-7.

757

758 Hong, Y., J. L. Haferman, W. S. Olson, and C. D. Kummerow, 2000: Microwave brightness
759 temperatures from tilted convective systems. *Journal of Applied Meteorology*, **39**(7), 983-998,
760 doi:10.1175/1520-0450(2000)039<0983:MBTFTC>2.0.CO;2.

761

762 Hong, Y., K. L. Hsu, S. Sorooshian, and X. Gao, 2004: Precipitation estimation from remotely
763 sensed imagery using an artificial neural network cloud classification system. *Journal of*
764 *Applied Meteorology*, **43**(12), 1834-1853, doi:10.1175/JAM2173.1.

765

766 Hou, A.Y., R.K. Kakar, S. Neeck, A. A. Azarbarzin, C. D. Kummerow, M. Kojima, R. Oki, K.
767 Nakamura, and T. Iguchi, 2014: The global precipitation measurement mission. *Bulletin of the*
768 *American Meteorological Society*, **95**(5), 701-722, doi:10.1175/BAMS-D-13-00164.1.

769

770 Hsu, K. L., X. Gao, S. Sorooshian, and H. V. Gupta, 1997: Precipitation estimation from
771 remotely sensed information using artificial neural networks. *Journal of Applied Meteorology*,
772 36(9), 1176-1190, doi:10.1175/1520-0450(1997)036<1176:PEFRSI>2.0.CO;2.

773

774 Huffman, G.J., D. T. Bolvin, D. Braithwaite, K. Hsu, R. Joyce, C. Kidd, E. J. Nelkin, S.
775 Sorooshian, J. Tan, and P. Xie, 2018: NASA global precipitation measurement (GPM)
776 integrated multi-satellite retrievals for GPM (IMERG). Algorithm theoretical basis document
777 v5.2, 31 pp, available at
778 https://pmm.nasa.gov/sites/default/files/document_files/IMERG_ATBD_V5.2_0.pdf.

779

780 Iguchi, T., and R. Meneghini, 2016a: GPM DPR Ku Precipitation Profile 2A 1.5 hours 5 km
781 V06, Goddard Earth Sciences Data and Information Services Center (GES DISC), accessed on
782 2019-11-01, doi:10.5067/GPM/DPR/Ku/2A/06.

783

784 Iguchi, T., and R. Meneghini, 2016b. GPM GMI (GPROF) Radiometer Precipitation Profiling
785 L2A 1.5 hours 13 km V05, Goddard Earth Sciences Data and Information Services Center (GES
786 DISC), Accessed on 2019-11-01, doi:10.5067/GPM/GMI/GPM/GPROF/2A/05.

787

788 Imaoka, K., T. Maeda, M. Kachi, M. Kasahara, N. Ito, and K. Nakagawa, 2012: Status of
789 AMSR2 instrument on GCOM-W1. In *Earth Observing Missions and Sensors: Development,*
790 *Implementation and Characterization*, ed. International Society for Optics and Photonics,
791 doi:10.1117/12.977774.

792

793 Kidd, C., T. Matsui, J. Chern, K. Mohr, C. Kummerow, and D. Randel, 2016: Global
794 precipitation estimates from cross-track passive microwave observations using a physically
795 based retrieval scheme. *Journal of Hydrometeorology*, **17**(1), 383-400, doi:10.1175/JHM-D-
796 15-0051.1.

797

798 Klein, C., D. Belušić, and C. M. Taylor, 2018: Wavelet scale analysis of mesoscale convective
799 systems for detecting deep convection from infrared imagery. *Journal of Geophysical*
800 *Research: Atmospheres*, **123**(6), 3035-3050, doi:10.1002/2017JD027432.

801

802 Kubota, T., S. Shige, H. Hashizume, K. Aonashi, N. Takahashi, S. Seto, M. Hirose, Y. N.
803 Takayabu, T. Ushio, K. Nakagawa, and K. Iwanami, 2007: Global precipitation map using
804 satellite-borne microwave radiometers by the GSMAp project: Production and validation. *IEEE*
805 *Transactions on Geoscience and Remote Sensing*, **45**(7), 2259-2275,
806 doi:10.1109/TGRS.2007.895337.

807

808 Kucera, P. A., W. F. Krajewski, and C. B. Young, 2004: Radar beam occultation studies using
809 GIS and DEM technology: An example study of Guam. *Journal of Atmospheric and Oceanic*
810 *Technology*, **21**(7), 995-1006, doi:10.1175/1520-0426(2004)021<0995:RBOSUG>2.0.CO;2.

811

- 812 Kumar, P., and E. Foufoula-Georgiou, 1997: Wavelet analysis for geophysical applications.
- 813 *Reviews of geophysics*, **35**(4), 385-412, doi:10.1029/97RG00427.
- 814
- 815 Kummerow, C. and L. Giglio: A passive microwave technique for estimating rainfall and
- 816 vertical structure information from space. Part I: Algorithm description. *Journal of Applied*
- 817 *Meteorology*, **33**(1), 3-18, doi:10.1175/1520-0450(1994)033<0003:APMTFE>2.0.CO;2.
- 818
- 819 Kummerow, C., W. S. Olson, and L. Giglio, 1996: A simplified scheme for obtaining
- 820 precipitation and vertical hydrometeor profiles from passive microwave sensors. *IEEE*
- 821 *Transactions on Geoscience and Remote Sensing*, **34**(5), 1213-1232, doi:10.1109/36.536538.
- 822
- 823 Kummerow, C., J. Simpson, O. Thiele, W. Barnes, A. T. C. Chang, E. Stocker, E., R. F. Adler,
- 824 A. Hou, R. Kakar, F. Wentz, and P. Ashcroft, 2000: The status of the Tropical Rainfall
- 825 Measuring Mission (TRMM) after two years in orbit. *Journal of Applied meteorology*, **39**(12),
- 826 1965-1982, doi:10.1175/1520-0450(2001)040<1965:TSOTTR>2.0.CO;2.
- 827
- 828 Kummerow, C., Y. Hong, W. S. Olson, S. Yang, R. F. Adler, J. McCollum, R. Ferraro, G. Petty,
- 829 D. B. Shin, and T. T. Wilheit, 2001: The evolution of the Goddard Profiling Algorithm
- 830 (GPROF) for rainfall estimation from passive microwave sensors. *Journal of Applied*
- 831 *Meteorology*, **40**(11), 1801-1820,
- 832 doi:10.1175/1520-0450(2001)040<1801:TEOTGP>2.0.CO;2.
- 833
- 834 Kummerow, C., W. Berg, J. Thomas-Stahle, and H. Masunaga, 2006: Quantifying global
- 835 uncertainties in a simple microwave rainfall algorithm. *Journal of Atmospheric and Oceanic*
- 836 *Technology*, **23**(1), 23-37, doi:10.1175/JTECH1827.1.

837

838 Kummerow, C.D., D. L. Randel, M. Kulie, N. Y. Wang, R. Ferraro, J. S. Munchak, and V.
839 Petkovic, 2015: The evolution of the Goddard profiling algorithm to a fully parametric scheme.
840 *Journal of Atmospheric and Oceanic Technology*, **32**(12), 2265-2280, doi:10.1175/JTECH-D-
841 15-0039.1.

842

843 Kunkee, D. B., G. A. Poe, D. J. Boucher, S. D. Swadley, Y. Hong, J. E. Wessel, and E. A.
844 Uliana, 2008: Design and evaluation of the first special sensor microwave imager/sounder.
845 *IEEE Transactions on Geoscience and Remote Sensing*, **46**(4), 863-883,
846 doi:10.1109/TGRS.2008.917980.

847

848 Lebsack, M.D., and T.S. L'Ecuyer, 2011: The retrieval of warm rain from CloudSat. *Journal of*
849 *Geophysical Research: Atmospheres*, **116**(D20), doi:10.1029/2011JD016076.

850

851 Lecun, Y., Y. Bengio, and G. Hinton, 2015: Deep learning. *Nature*, **521**, 436-444,
852 doi:10.1038/nature14539.

853

854 Liu, G. and J. A. Curry, 1992: Retrieval of precipitation from satellite microwave measurement
855 using both emission and scattering. *Journal of Geophysical Research: Atmospheres*, **97**(D9),
856 9959-9974, doi:10.1029/92JD00289.

857

858 Liu, C. and E.J. Zipser, 2009: "Warm rain" in the tropics: Seasonal and regional distributions
859 based on 9 yr of TRMM data. *Journal of Climate*, **22**(3), 767-779,
860 doi:10.1175/2008JCLI2641.1.

861

862 Löhner, U., S Crewell, C. Simmer, and A. Macke, A., 2001: Profiling cloud liquid water by
863 combining active and passive microwave measurements with cloud model statistics. *Journal of*
864 *Atmospheric and Oceanic Technology*, **18**(8), 1354-1366, doi:10.1175/1520-
865 0426(2001)018<1354:PCLWBC>2.0.CO;2.

866

867 Milligan, P. R., and P. J. Gunn, 1997: Enhancement and presentation of airborne geophysical
868 data. *AGSO Journal of Australian Geology and Geophysics*, **17**(2), 63-75.

869

870 Mugnai, A., E. A. Smith, G. J. Tripoli, B. Bizzarri, D. Casella, S. Dietrich, F. Di Paola, G.
871 Panegrossi, and P. Sanò, 2013: CDRD and PNPR satellite passive microwave precipitation
872 retrieval algorithms: EuroTRMM/EURAINSAT origins and H-SAF operations. *Natural*
873 *Hazards and Earth System Sciences*, **13**(4), 887-912, doi:10.5194/nhess-13-887-2013.

874

875 Munchak, S. J., and G. Skofronick-Jackson, 2013: Evaluation of precipitation detection over
876 various surfaces from passive microwave imagers and sounders. *Atmospheric research*, **131**,
877 81-94, doi:10.1016/j.atmosres.2012.10.011.

878

879 Nogueira, K., O. A. Penatti, and J. A. dos Santos, J. 2017: Towards better exploiting
880 convolutional neural networks for remote sensing scene classification. *Pattern Recognition*, **61**,
881 539-556, doi:doi.org/10.1016/j.patcog.2016.07.001.

882

883 Petković, V., C. D. Kummerow, D. L. Randel, J. R. Pierce, and J. K. Kodros, 2018: Improving
884 the quality of heavy precipitation estimates from satellite passive microwave rainfall retrievals.
885 *Journal of Hydrometeorology*, **19**(1), 69-85, doi:10.1175/JHM-D-17-0069.1.

886

887 Petty, G.W., 1994: Physical retrievals of over-ocean rain rate from multichannel microwave
888 imagery. Part II: Algorithm implementation. *Meteorology and Atmospheric Physics*, **54**(1-4),
889 101-121, doi:10.1007/BF01030054.

890

891 Petty, G. W., and K. Li, 2013: Improved passive microwave retrievals of rain rate over land and
892 ocean. Part I: Algorithm description. *Journal of Atmospheric and Oceanic Technology*, **30**(11),
893 2493-2508, doi:10.1175/JTECH-D-12-00144.1.

894

895 Petty, G.W. and R. Bennartz, 2017: Field-of-view characteristics and resolution matching for
896 the Global Precipitation Measurement (GPM) Microwave Imager (GMI). *Atmospheric
897 Measurement Techniques*, **10**(3), 745-758, doi:10.5194/amt-10-745-2017.

898

899 Prabhakara, C., R. Iacovazzi Jr., J.A. Weinman and G. Dalu, 2000: A TRMM microwave
900 radiometer rain rate estimation method with convective and stratiform discrimination. *Journal
901 of the Meteorological Society of Japan*, **78**(3), 241-258, doi:10.2151/jmsj1965.78.3_241.

902

903 Ringerud, S., C. D. Kummerow, and C. D. Peters-Lidard, 2015: A prototype physical database
904 for passive microwave retrievals of precipitation over the US Southern Great Plains. *Journal of
905 Geophysical Research: Atmospheres*, **120**(19), 10465-10482, doi:10.1002/2015JD023430.

906

907 Sanò, P., D. Casella, A. Mugnai, G. Schiavon, E. A. Smith, and G. J. Tripoli, 2013:
908 Transitioning from CRD to CDRD in Bayesian retrieval of rainfall from satellite passive
909 microwave measurements: Part 1. Algorithm description and testing. *IEEE Transactions on
910 Geoscience and Remote Sensing*, **51**(7), 4119-4143, doi:10.1109/TGRS.2012.2227332.

911

912 Sanò, P., G. Panegrossi, D. Casella, F. Di Paola, L. Milani, A. Mugnai, M. Petracca, and S.
913 Dietrich, 2015: The Passive microwave Neural network Precipitation Retrieval (PNPR)
914 algorithm for AMSU/MHS observations: description and application to European case studies.
915 *Atmospheric Measurement Techniques*, **8**(2), 837-857, doi:10.5194/amt-8-837-2015.

916
917 Skofronick-Jackson, G., W. A. Petersen, W. Berg, C. Kidd, E. F. Stocker, D. B. Kirschbaum,
918 R. Kakar, S. A. Braun, G. J. Huffman, T. Iguchi, and P. E. Kirtstetter, 2017: The Global
919 Precipitation Measurement (GPM) mission for science and society. *Bulletin of the American
920 Meteorological Society*, **98**(8), 1679-1695, doi:10.1175/BAMS-D-15-00306.1.

921
922 Skofronick-Jackson, G., W. Berg, C. Kidd, D. B. Kirschbaum, W. A. Petersen, G. J. Huffman,
923 and Y. N. Takayabu, 2018: Global Precipitation Measurement (GPM): Unified Precipitation
924 Estimation from Space. In *Remote Sensing of Clouds and Precipitation*, C. Andronache, ed.
925 Springer, 175-193, doi:10.1007/978-3-319-72583-3_7.

926
927 Spencer, R. W., 1986: A satellite passive 37-GHz scattering-based method for measuring
928 oceanic rain rates. *Journal of climate and applied meteorology*, **25**(6), 754-766.
929 doi:10.1175/1520-0450(1986)025<0754:ASPGSB>2.0.CO;2.

930
931 Spencer, R.W., H. M. Goodman, and R. E. Hood, 1989: Precipitation retrieval over land and
932 ocean with the SSM/I: Identification and characteristics of the scattering signal. *Journal of
933 Atmospheric and Oceanic Technology*, **6**(2), 254-273, doi:10.1175/1520-
934 0426(1989)006<0254:PROLAO>2.0.CO;2.

935

936 Szeliski, R., 2010: *Computer vision: algorithms and applications*. ed. Springer, 812 pp,
937 doi:10.1007/978-1-84882-935-0.

938

939 Takbiri, Z., A. Ebtehaj, E. Foufoula-Georgiou, P. E. Kirtetter, and F. J. Turk, 2019: A
940 prognostic retrieval approach for microwave precipitation phase detection over snow cover.
941 *Journal of Hydrometeorology*, doi:10.1175/JHM-D-18-0021.1.

942

943 Tapiador, F. J., R. Moreno, and Z. S. Haddad, 2018: Estimates of the precipitation top heights
944 in convective systems using microwave radiances. *IEEE Transactions on Geoscience and*
945 *Remote Sensing*, doi:10.1109/TGRS.2018.2882002.

946

947 Tokay, A., D. A. Short, C. R. Williams, W. L. Ecklund, and K. S. Gage, 1999: Tropical rainfall
948 associated with convective and stratiform clouds: Intercomparison of disdrometer and profiler
949 measurements. *Journal of Applied Meteorology*, **38**(3), 302-320, doi:10.1175/1520-
950 0450(1999)038<0302:TRAWCA>2.0.CO;2

951

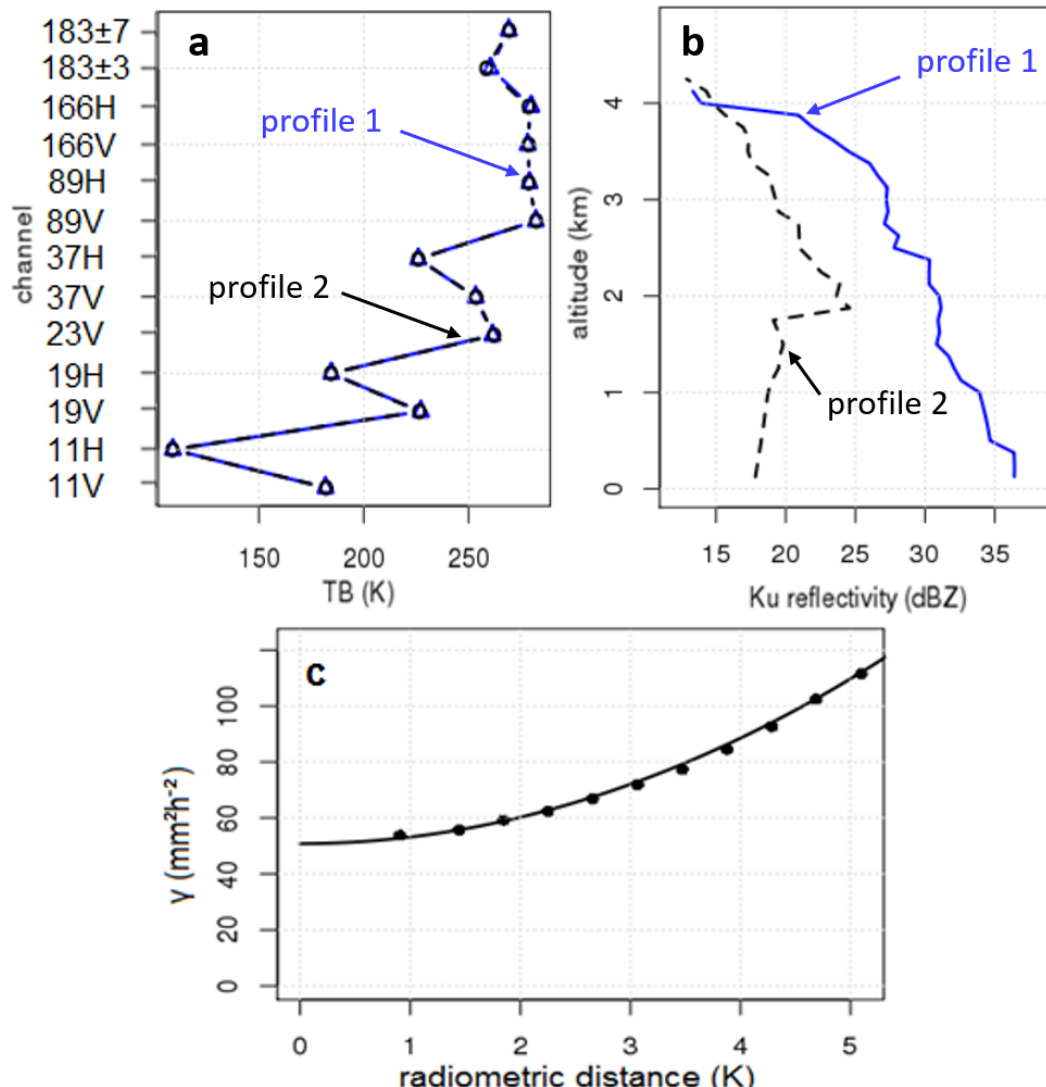
952 Tsintikidis, D., J. L. Haferman, E. N. Anagnostou, W. F. Krajewski, and T. F. Smith, 1997: A
953 neural network approach to estimating rainfall from spaceborne microwave data. *IEEE*
954 *Transactions on Geoscience and Remote Sensing*, **35**(5), 1079-1093, doi:10.1109/36.628775.

955

956 Turiel, A., J. Grazzini, and H. Yahia, 2005: Multiscale techniques for the detection of
957 precipitation using thermal IR satellite images. *IEEE Geoscience and Remote Sensing Letters*,
958 **2**(4), 447-450, doi:10.1109/LGRS.2005.852712.

959

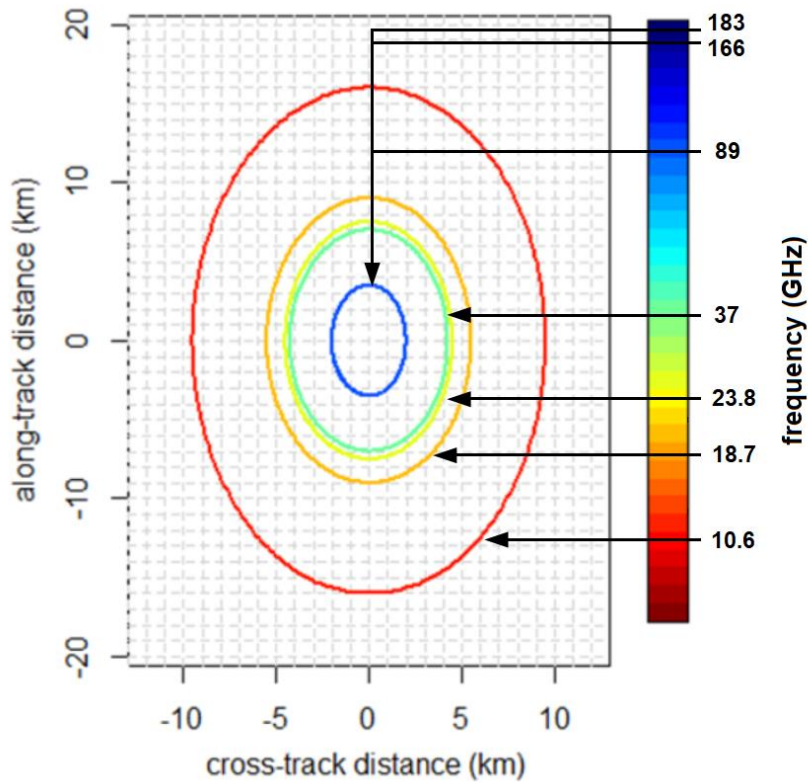
- 960 Ushio, T., K. Sasashige, T. Kubota, S. Shige, K. I. Okamoto, K. Aonashi, T. Inoue, N.
961 Takahashi, T. Iguchi, M. Kachi, and R. Oki, 2009: A Kalman filter approach to the Global
962 Satellite Mapping of Precipitation (GSMaP) from combined passive microwave and infrared
963 radiometric data. *Journal of the Meteorological Society of Japan*. **87**, 137-151,
964 doi:10.2151/jmsj.87A.137.
- 965
- 966 Wilheit, T., and A. T. C. Chang, 1980: An algorithm for retrieval of ocean surface and
967 atmospheric parameters from the observations of the scanning multichannel microwave
968 radiometer. *Radio Science*, **15**(3), 525-544, doi:10.1029/RS015i003p00525.
- 969
- 970 Wilheit, T. T., A. T. Chang, and L. S. Chiu, 1991: Retrieval of monthly rainfall indices from
971 microwave radiometric measurements using probability distribution functions. *Journal of*
972 *Atmospheric and Oceanic Technology*, **8**(1), 118-136, doi:10.1175/1520-
973 0426(1991)008<0118:ROMRIF>2.0.CO;2.
- 974
- 975 Xie, P., R. Joyce, S. Wu, S. H. Yoo, Y. Yarosh, F. Sun, and R. Lin, 2017: Reprocessed, bias-
976 corrected CMORPH global high-resolution precipitation estimates from 1998. *Journal of*
977 *Hydrometeorology*, **18**(6), 1617-1641, doi:10.1175/JHM-D-16-0168.1.
- 978
- 979 You, Y., N. Y. Wang, and R. Ferraro, 2015: A prototype precipitation retrieval algorithm over
980 land using passive microwave observations stratified by surface condition and precipitation
981 vertical structure. *Journal of Geophysical Research: Atmospheres*, **120**(11), 5295-5315,
982 doi:10.1002/2014JD0225343.



983

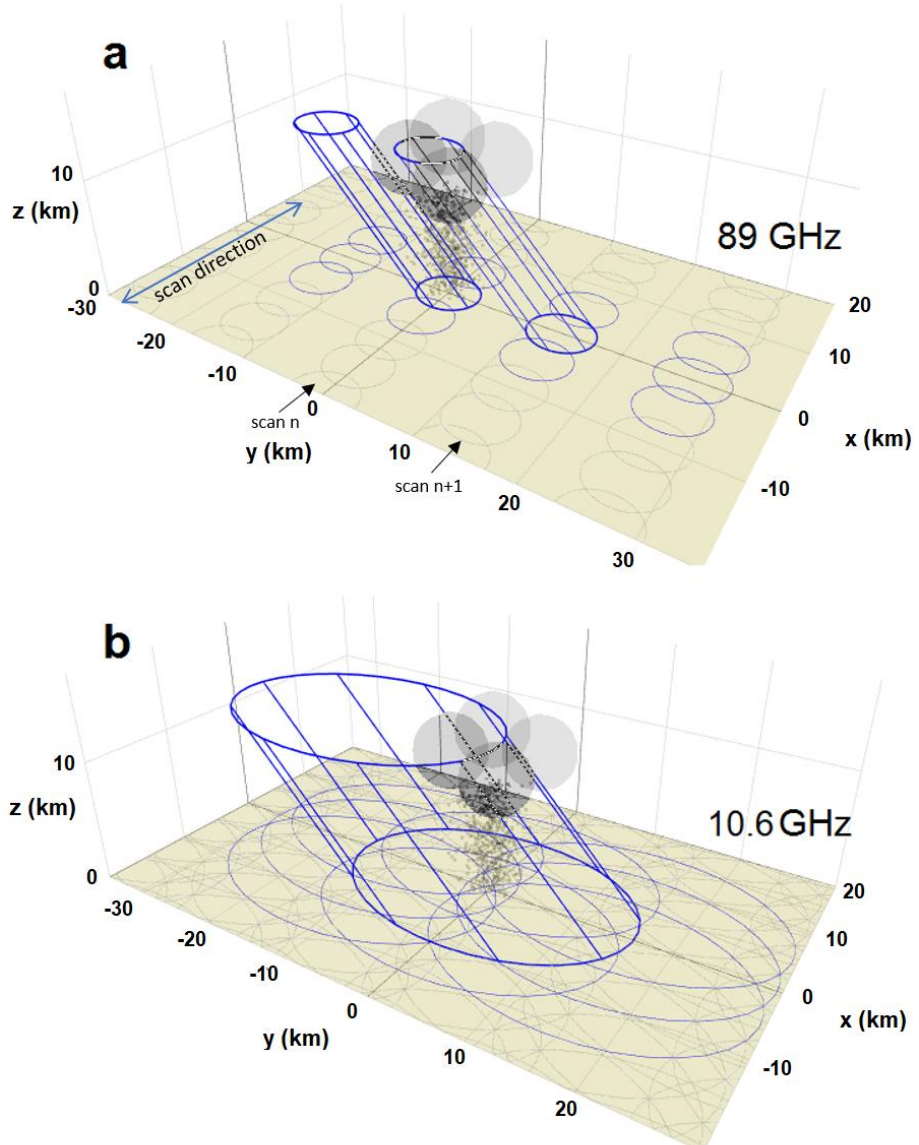
984 Figure 1: Atmospheric profiles with quasi-identical spectral signatures can have very different
 985 radar reflectivity profiles and surface rain rates. (a) Two spectral signatures measured by GMI
 986 over ocean and (b) corresponding Ku reflectivities measured by the DPR along GMI's field of
 987 view. The profile 1 was observed at latitude -3.29° and longitude 170.89° on 2016-09-06 at
 988 12:10 UTC (orbit #14342 of the GPM Core observatory) and has a 15 mm/h surface
 989 precipitation rate. The profile 2 was observed at latitude 2.49° and longitude -136.25° on 2015-
 990 12-04 at 17:30 UTC (orbit #10036) and has a 1 mm/h surface precipitation rate. (c) Variogram
 991 of the function $R(\mathbf{TB})$ in the 13-dimensional space of TBs derived from 4000 collocated GMI-
 992 measured radiometric vectors \mathbf{TB}_i (all within a 5 K radiometric distance from the two vectors

993 shown in the panel a) and DPR-derived surface precipitation rate R_i over ocean. The variogram
994 shows the expected value γ of the squared difference $\frac{1}{2} \times |R(\mathbf{TB}_i) - R(\mathbf{TB}_j)|^2$ as a function
995 of the Euclidean distance $\|\mathbf{TB}_i - \mathbf{TB}_j\|$. The so-called “nugget effect” (expected squared
996 difference $|R(\mathbf{TB}_1) - R(\mathbf{TB}_2)|^2$ not tending toward zero when the distance $\|\mathbf{TB}_1 - \mathbf{TB}_2\|$
997 tends toward zero [Cressie 1993]) quantifies the inherent uncertainty of the retrieval and is
998 solely attributed to the limited radiometric information. The nugget effect accounts for 52% of
999 the variance of R among the 4000 hydrometeor profiles, the total sample variance being 98
1000 mm^2h^{-2} and the sample mean 13.1 mm/h.



1001

1002 Figure 2: -3dB footprints of GMI at 10.6, 18.7, 23.8, 37, 89, 166 and 183 GHz. Because of
 1003 varying footprints of the different GMI channels, defining the retrieval “pixel” and resolution
 1004 is not trivial. We note that same-frequency vertically and horizontally polarized channels have
 1005 identical footprints and that the 166 and 183 GHz channels have the same footprint size as the
 1006 89 GHz channels.

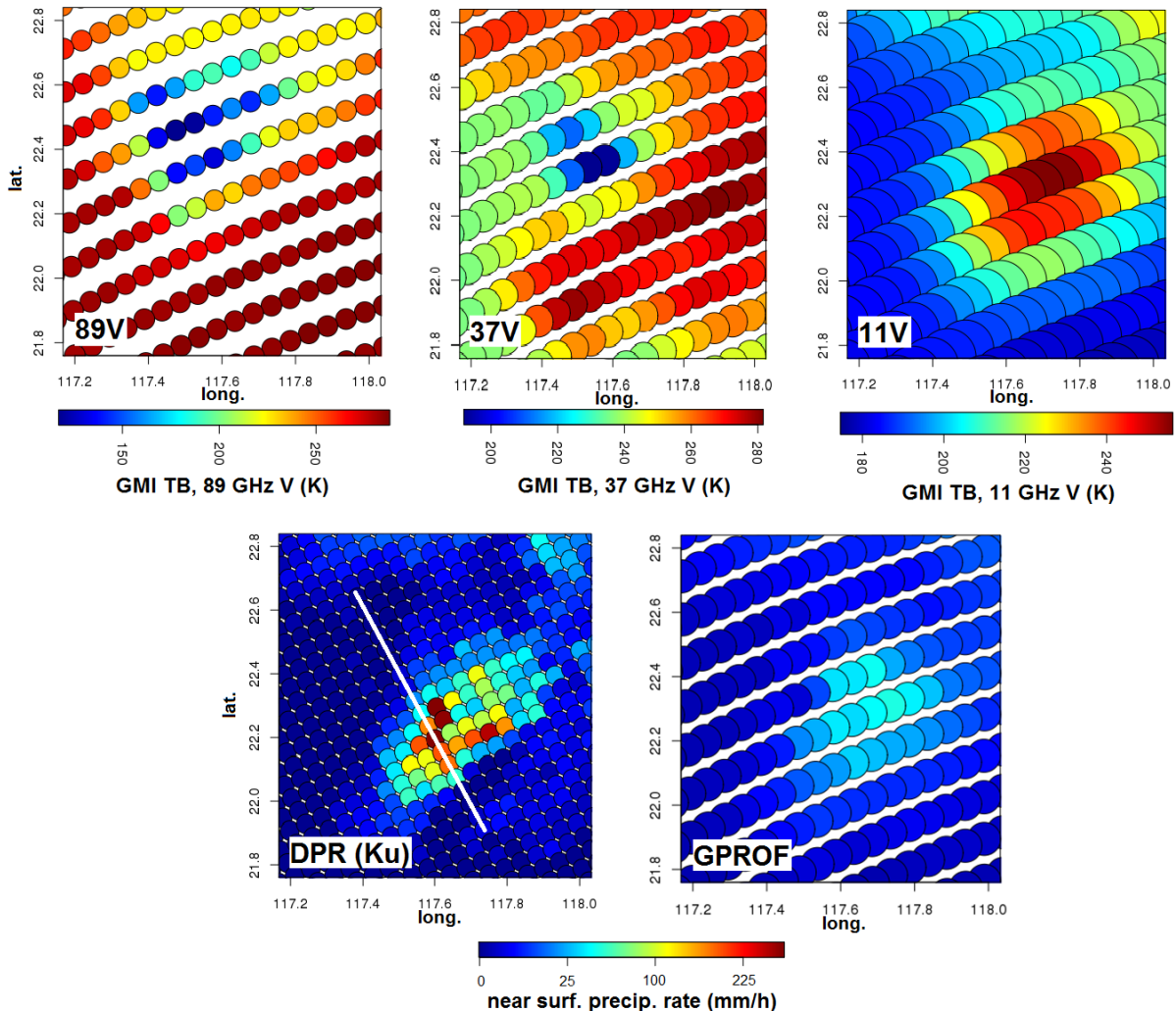


1007

1008 Figure 3: Illustration of split and shifted multispectral information from the observation
1009 geometry.

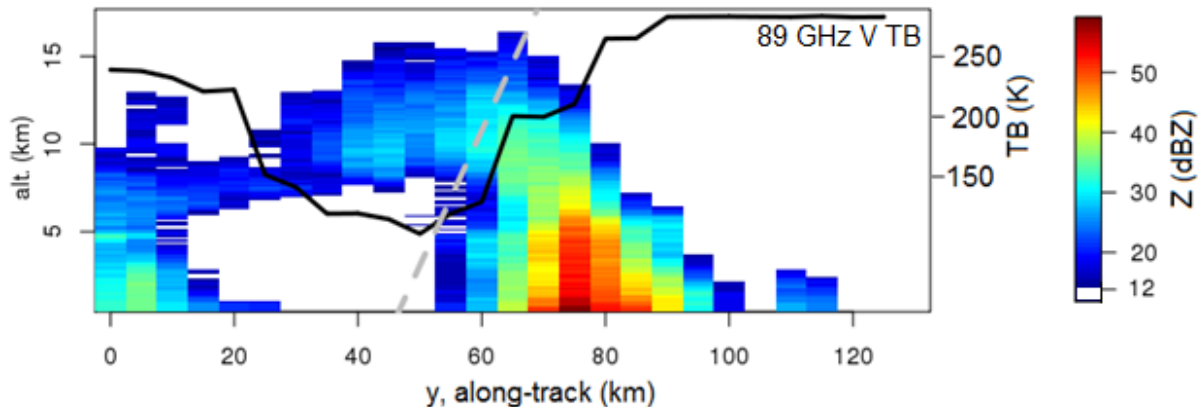
1010 (a) GMI three-dimensional observation geometry at 89 GHz. The cylinders correspond to the
1011 fields of view (-3 dB contour) of individual TB measurements. Here, two fields of view
1012 intercepting the same atmospheric column at different altitudes are represented. The footprints
1013 corresponding to several adjacent fields of view are shown on the surface.

1014 (b) GMI three-dimensional observation geometry at 10.6 GHz. With the overlapping of the
1015 fields of view, a single atmospheric column is intercepted up to 12 times at 10.6 GHz.



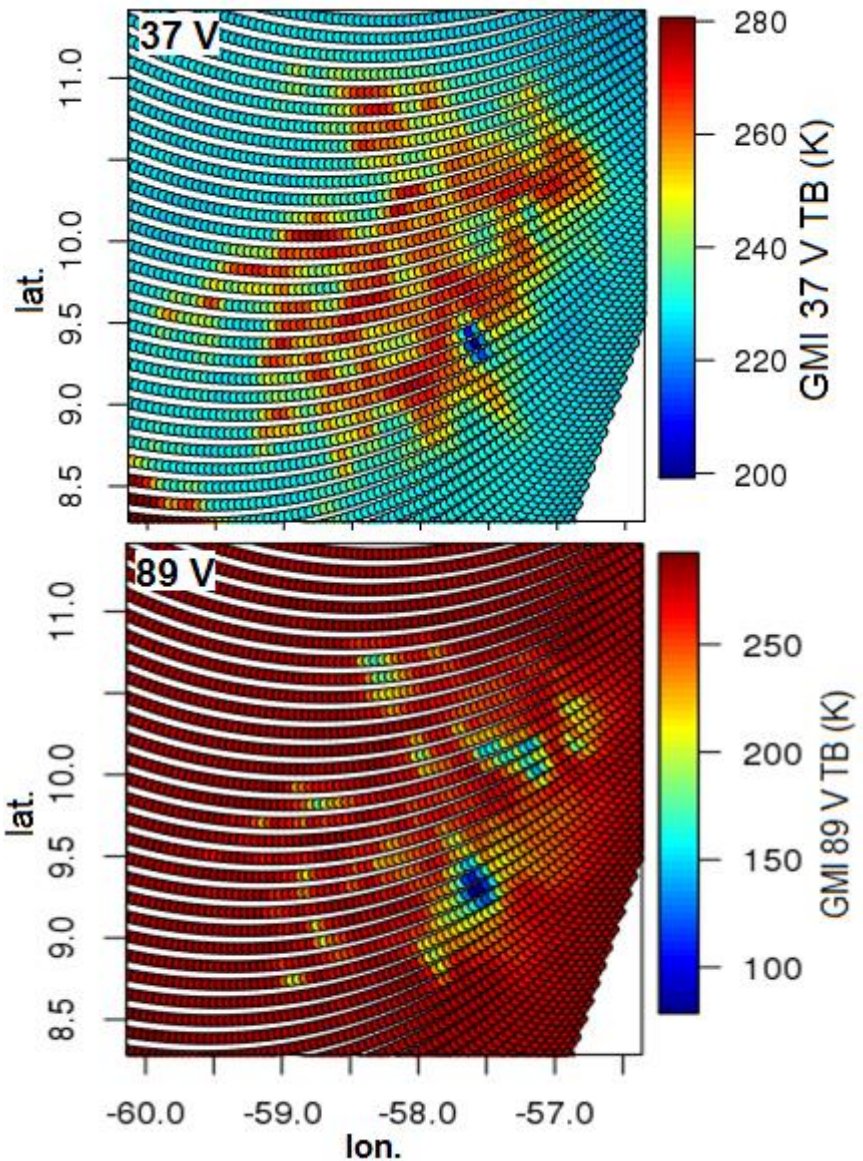
1016

1017 Figure 4: Exploration of the information in the spatial structure of the GMI TBs for an oceanic
 1018 convective system (South China Sea, 2016-10-09 at 04:45 UTC). (Top) Observed TBs at 89,
 1019 37 and 10.6 GHz (vertical polarization). (Bottom) Near-surface precipitation rates derived from
 1020 the DPR and from GMI using the GPROF algorithm; the white line corresponds to the cross
 1021 section shown in Figure 5. The ice scattering signature at 89 GHz is shifted to the North-West
 1022 relatively to the emission signature at 10.6 GHz; this shift and the spatial structure of the TB
 1023 fields in general reflect the three-dimensional structure of the precipitation field (see Figure 5).
 1024 This example illustrates the need to overcome pixel-wise relations between TBs and
 1025 precipitation by using the spatial information of the TB fields.



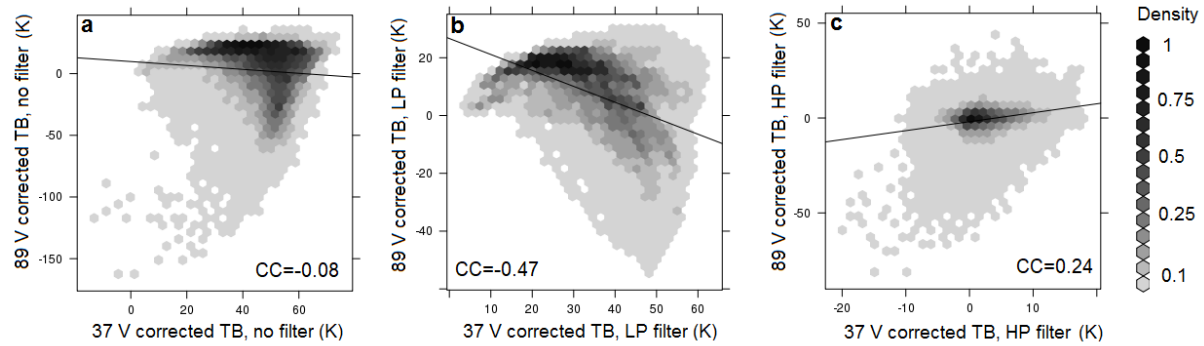
1026

1027 Figure 5: DPR Ku reflectivity vertical cross section of the precipitation system shown in Figure
 1028 4. The system is a tilted deep convective system. The cross section is taken along the azimuthal
 1029 direction of the GMI beams. The gray dashed line shows the direction of GMI's observations.
 1030 The black line shows GMI-measured 89 GHz V TB (scale on the right). The tilt amplifies the
 1031 parallax shift causing the spatial mismatch between the liquid drops emission signature and the
 1032 ice scattering signature in the TB fields.



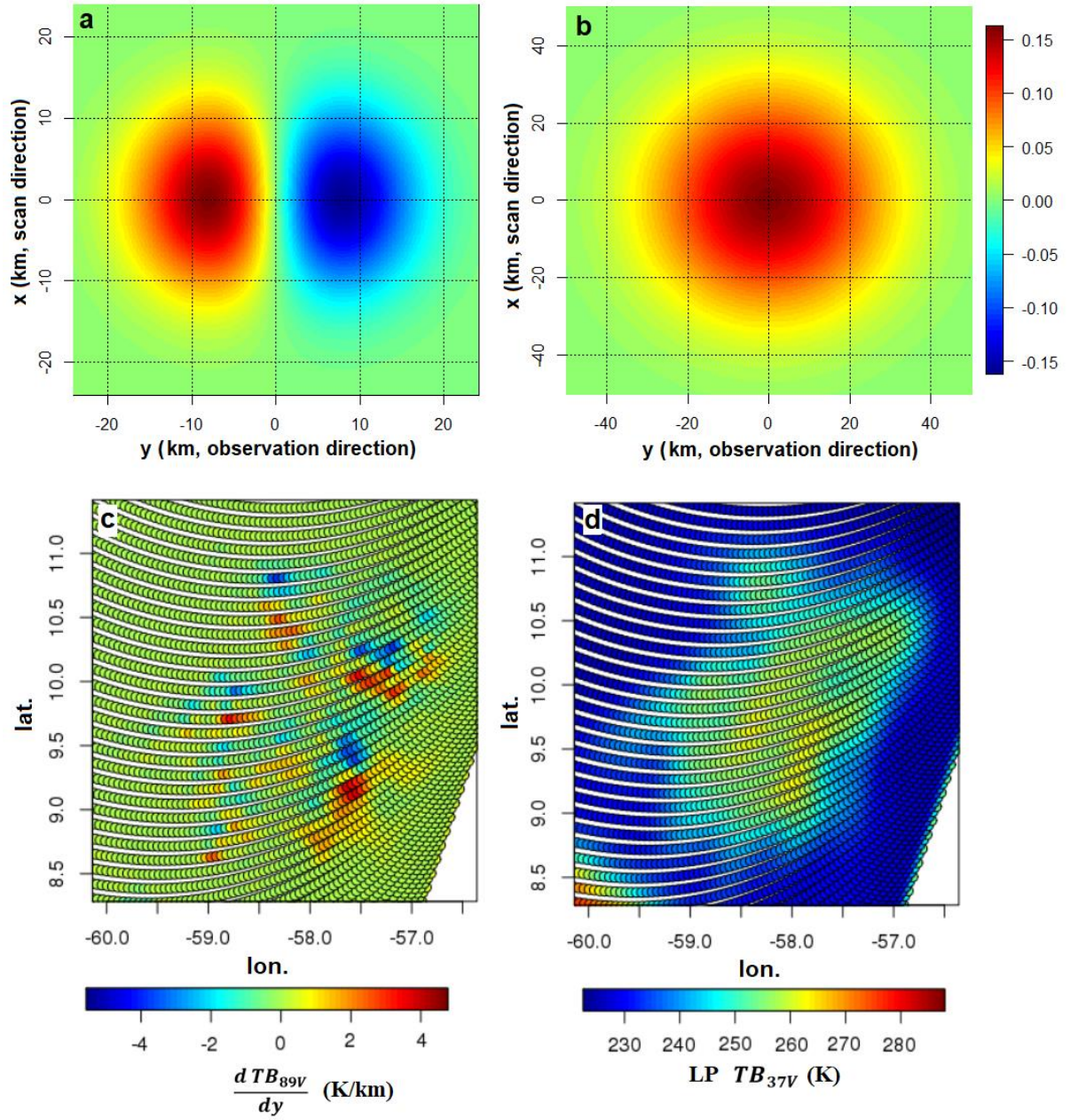
1033

1034 Figure 6: Mesoscale convective complex observed by GMI at 37 and 89 GHz (vertical
 1035 polarization) over the Atlantic Ocean on 2016-10-09 at 06:40 UTC. At 37 GHz the high TB
 1036 envelope marks the extent of the precipitating area. Inside this envelope, local depressions of
 1037 the TB at 89 and 37 GHz mark the most intense convective cells.



1038

1039 Figure 7: Scale dependence in the statistical relations between the 37V and 89V TBs in
 1040 precipitating areas over ocean. (a) Joint distribution of TBs 37V and 89V observed by GMI in
 1041 precipitating areas over ocean; (b) joint distribution of TBs 37V and 89V after low-pass spatial
 1042 filtering (convolution with a Gaussian kernel with $\sigma = 30$ km) of both TBs; and (c) joint
 1043 distribution of TBs 37V and 89V after high-pass spatial filtering (isotropic Laplacian of
 1044 Gaussian kernel with $\sigma = 15$ km) of both TBs. See Szeliski (2010) for the description of the
 1045 Gaussian and Laplacian of Gaussian kernels. The correlation between the 37V and 89V TBs is
 1046 negative for the coarse scale gradients and positive for the fine-scale gradients. The correlation
 1047 coefficients are computed from 70 000 randomly sampled independent data points over global
 1048 ocean and are all statistically significant at the 99% level. All TBs are corrected for surface
 1049 temperature variations before applying the filtering (see appendix B and Guilloteau et al. 2018).



1050

1051 Figure 8: Convolution kernels used to extract spatial information from the TB fields.

1052 (a) First derivative of Gaussian kernel [Szeliski, 2010]: $f(x,y) = -\frac{y}{2\pi\sigma^4} e^{-\frac{x^2+y^2}{2\sigma^2}}$ with $\sigma =$

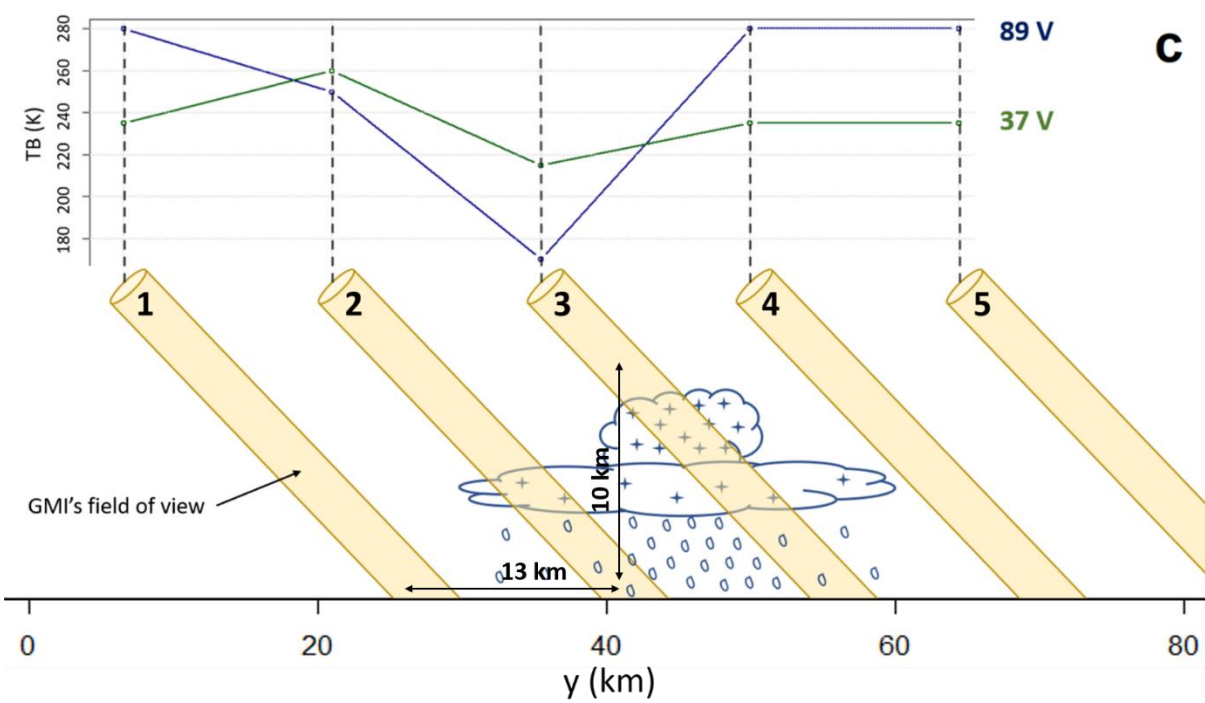
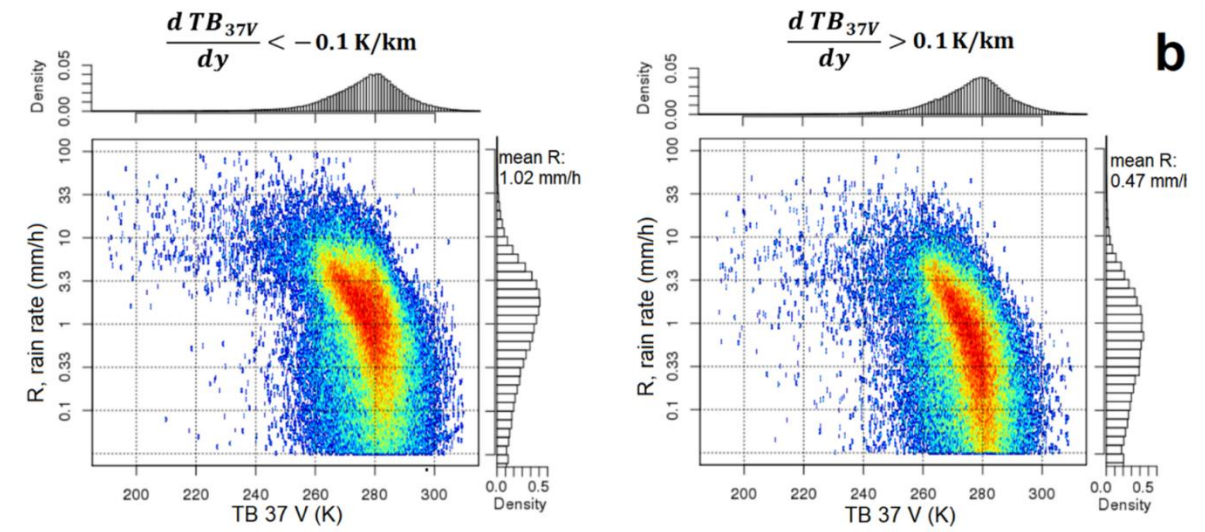
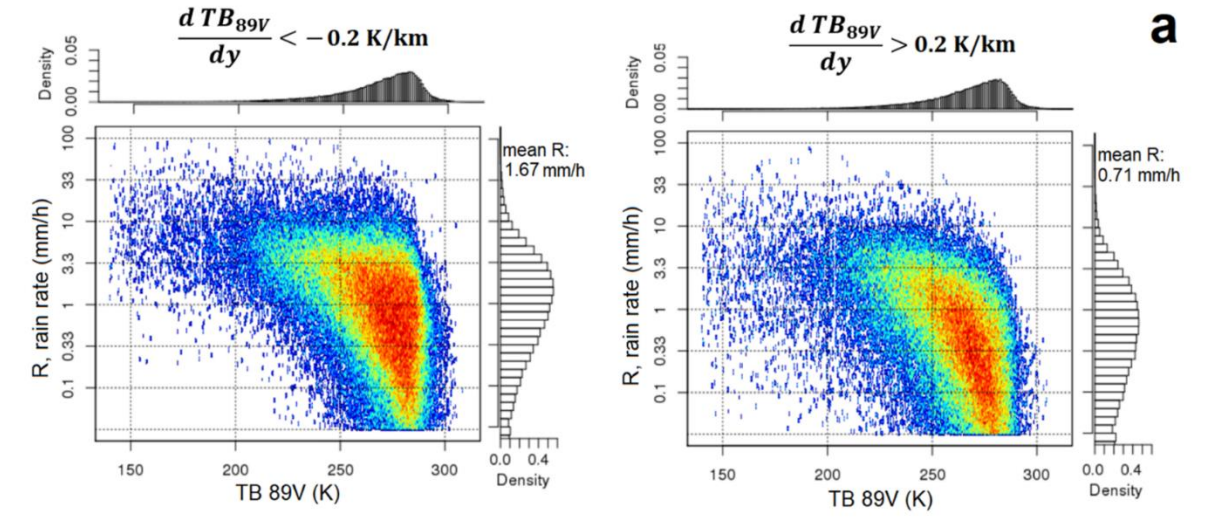
1053 8 km; this kernel is convolved with the 37V and 89V TB fields. (b) Gaussian kernel [Szeliski,

1054 2010]: $f(x,y) = \frac{1}{2\pi\sigma^2} e^{-\frac{x^2+y^2}{2\sigma^2}}$ with $\sigma = 20$ km; this kernel is convolved with the 37 V TB

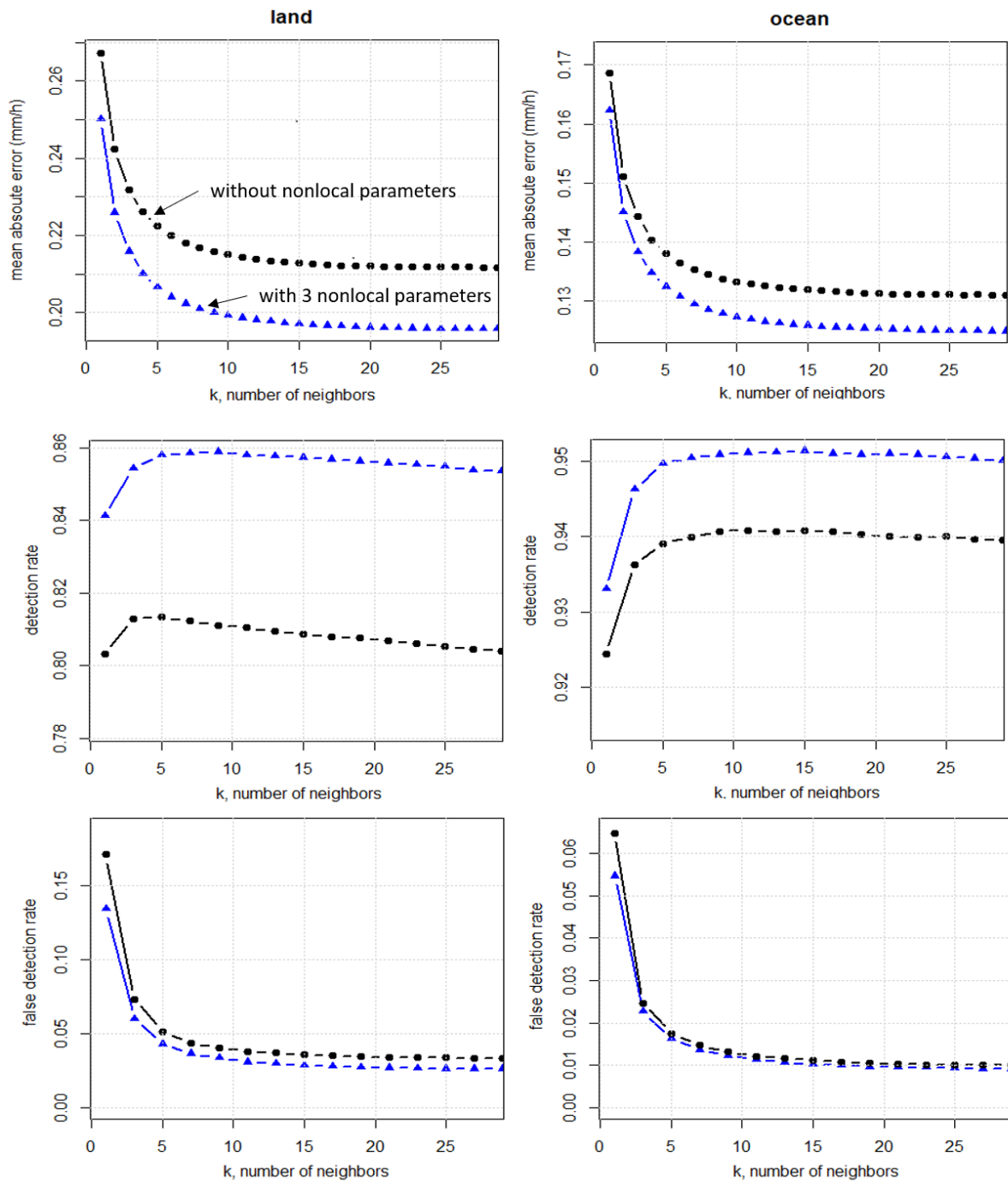
1055 field. (c) Result of the convolution of the 89V TB field shown in Figure 6 (bottom) with the

1056 First derivative of Gaussian kernel. (d) Result of the convolution of the 37V TB field shown in

1057 Figure 6 (top) with the Gaussian kernel. The Gaussian smoothing kernel partially erases the ice-
1058 scattering signal at 37 GHz. In panels (a) and (b), the x direction is tangent to the imager's scan
1059 (orthogonal to the observation direction) and the y direction is along the azimuthal direction of
1060 the imager's observation beam (orthogonal to the scan).



1062 Figure 9: (a) Joint distributions of DPR surface rain rates and collocated GMI 89V TBs
1063 conditioned on the value of the spatial derivative (gradient) of the 89V TB in the azimuthal
1064 direction of GMI's observation beam over land: for negative (left), and positive (right)
1065 gradients. (b) Joint distributions of DPR surface rain rates and collocated GMI 37V TBs
1066 conditioned on the value of the spatial derivative (gradient) of the 37V TB in the azimuthal
1067 direction of GMI's observation beam over land: for negative (left), and positive (right)
1068 gradients. (c) Schematic illustration of GMI's observation geometry for a typical convective
1069 system. The observation geometry causes the asymmetrical relationship between TB gradients
1070 and precipitation rates at 37 and 89 GHz. The area of maximum precipitation rate (between the
1071 fields of view 2 and 3) corresponds to decreasing TB gradients along the observation direction.
1072 The distributions of panels (a) and (b) are obtained from 700 000 randomly sampled collocated
1073 DPR and GMI observations over vegetated surfaces (coastal areas and snow-covered areas
1074 excluded). Precipitation rates correspond to near-surface KuPR-derived precipitation rates
1075 averaged inside GMI's -3 dB footprint at 18.7 GHz.

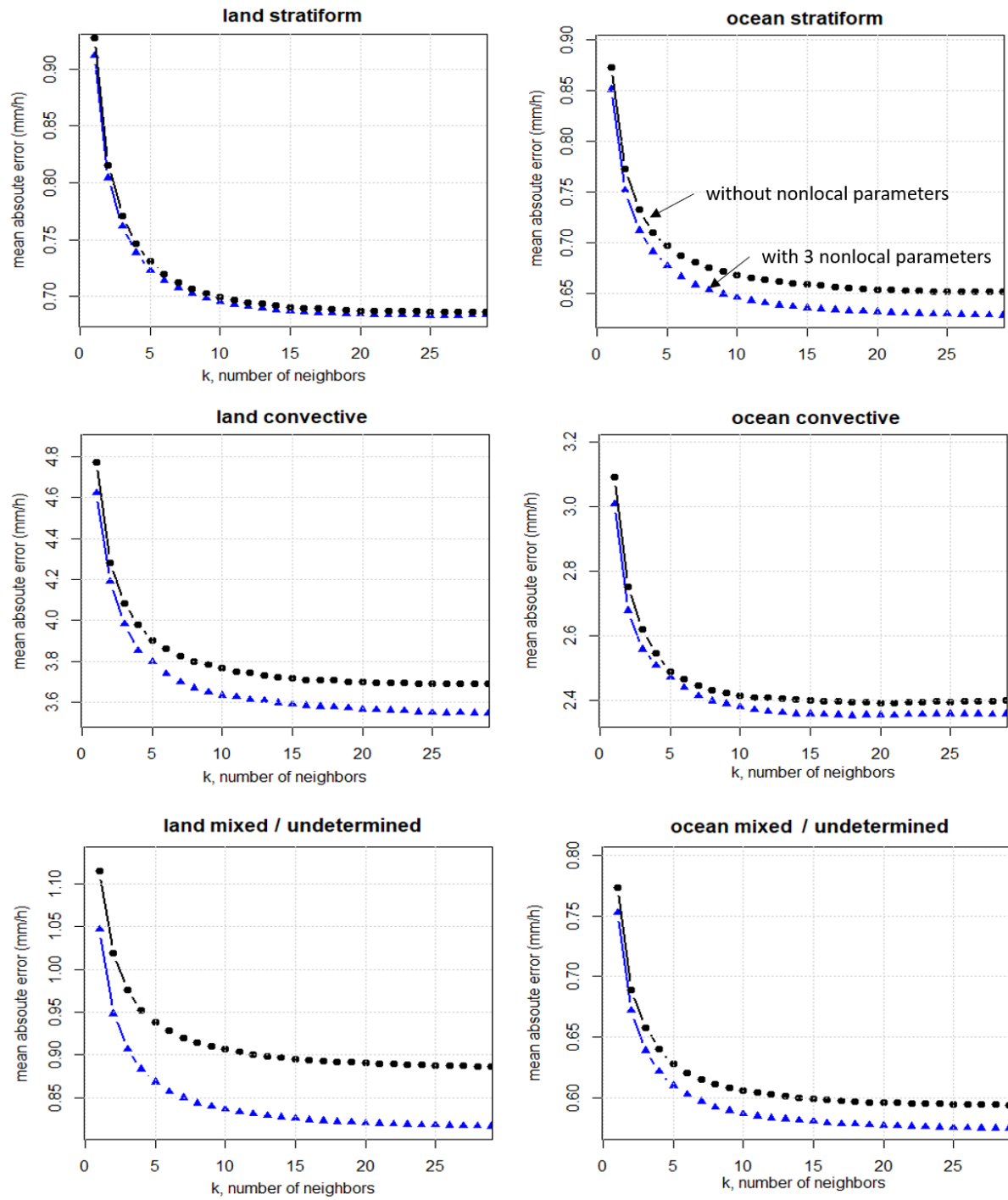


1076

1077 Figure 10: Comparison of the retrieval performance of the k -nearest neighbors algorithm with
 1078 and without the nonlocal parameters.

1079 (Top) Mean absolute error of the retrieved near-surface precipitation rate over land and ocean
 1080 as a function of the number k of neighbors retained in the nearest-neighbor algorithm for two
 1081 different retrieval schemes: using 13 TBs plus the 2-m temperature (black circles); and using
 1082 13 TBs plus the 2-m temperature plus 3 nonlocal radiometric parameters (blue triangles).

1083 (Middle) Detection rate over land and ocean as a function of k with (blue triangles) and without
1084 (black circles) the three nonlocal radiometric parameters. (Bottom) False detection rate over
1085 land and ocean as a function of k with (blue triangles) and without (black circles) the three
1086 nonlocal radiometric parameters. The three nonlocal parameters are the spatial derivative of the
1087 37V and 89V TBs in the azimuthal direction of the beam (from a first derivative of Gaussian
1088 convolution kernel with $\sigma = 8$ km) and the low-pass filtered 37V TB (using a smoothing
1089 Gaussian convolution kernel with $\sigma = 20$ km). Note that the detection rate and false detection
1090 rate are computed only for odd values of k .



1091

1092 Figure 11: Mean absolute error of the retrieved near-surface precipitation rate over land (left)
 1093 and ocean (right), for stratiform (top), convective (middle) and mixed / undetermined (bottom)
 1094 hydrometeor profiles, as a function of the number k of neighbors retained by the nearest-
 1095 neighbor algorithm for two different retrieval schemes: using 13 TBs plus the 2-m temperature
 1096 (black circles); and using 13 TBs plus the 2-m temperature plus 3 nonlocal radiometric

1097 parameters (blue triangles). The number of stratiform, convective and mixed / undetermined
1098 profiles is respectively 301934, 30931, 188657 over land, and 233194, 21133, 172254 over
1099 ocean. The class of hydrometeor profile is determined from the KuPR reflectivity profile using
1100 the Awaka et al. (1997) method. A profile is classified as stratiform (convective) if 60% or more
1101 of the 18.7 GHz footprint is classified as stratiform (convective). All other precipitating profiles
1102 are classified as mixed or undetermined precipitation type.